BNL-229676-2026-JAAM

Adsorption-based direct air capture using hierarchical porous composites prepared via confined-space crystallization

G. del Valle-Pérez, K. T. Kisslinger

To be published in "Chemical Engineering Journal"

February 2026

Center for Functional Nanomaterials

Brookhaven National Laboratory

U.S. Department of Energy

USDOE Office of Science (SC), Basic Energy Sciences (BES). Scientific User Facilities (SUF)

DISCLAIMER

Adsorption-Based Direct Air Capture Using Hierarchical Porous Composites Prepared via Confined-Space Crystallization

Gabriela C. del Valle-Pérez[1], Juan Carlos Muñoz-Senmache[1], Sebastián Espiña-Santiago[1], Erick M. Mendez-Rios[1], Kim Kisslinger[2], and Arturo J. Hernández-Maldonado[1*]

[1]Department of Chemical Engineering, University of Puerto Rico Mayagüez Campus, Mayagüez, Puerto Rico 00680, USA

[2] Center for Functional Nanomaterials, Brookhaven National Laboratory, Upton, NY 11973

* To whom correspondence should be addressed. Email: arturoj.hernandez@upr.edu

ORCID IDs:

del Valle-Pérez: 0000-0002-2860-6931

Muñoz-Senmache: 0000-0003-2437-275X

Kisslinger: 0000-0002-6528-7044

Hernández-Maldonado: 0000-0001-9379-8987

Abstract

Capturing CO_2 at trace concentration remains a critical challenge in sustainable carbon management via adsorption, as conventional adsorbents suffer from low CO_2 selectivity, poor moisture tolerance, and energy-intensive regeneration requirements. Here, we report a hierarchical Ba^{2+}-exchanged silicoaluminophosphate (Ba^{2+}-CSAPO-34) composite synthesized via confined-space crystallization within an activated carbon matrix. Comprehensive characterization revealed a confined nucleation mechanism and the successful incorporation of Ba^{2+} active sites within the SAPO-34 framework, achieved via a two-step liquid ion-exchange protocol. The core-shell architecture combines the selective CO_2 binding of Ba^{2+}-functionalized SAPO-34 with the hydrophobic protection of the carbon shell. Fixed-bed adsorption tests demonstrated strong CO_2 binding (at 500–2500 ppm), no roll-up, and effective suppression of water affinity, while maintaining high selectivity even at 90% relative humidity. A phenomenological adsorption model, validated against dynamic breakthrough data, accurately predicted dynamic adsorption behavior under real-world operating conditions, enabling rational process design for direct air capture (DAC) and closed-loop life support systems. These results establish Ba^{2+}-CSAPO-34 as a scalable, moisture-resistant adsorbent that addresses key limitations in trace CO_2 capture, advancing practical implementation of carbon removal technologies.

Keywords: *hierarchical composite, adsorption, carbon dioxide, water, hydrophobic, direct air capture*

1. Introduction

More than 37 billion tons of carbon dioxide are generated anthropogenically and emitted into the atmosphere each year [1, 2]. To address the complex problem of remediation, it is not sufficient to rely solely on reducing CO_2 emissions; more targeted, feasible solutions, such as direct air capture (DAC), are required [3-5]. However, removing CO_2 at trace concentrations (400–1000 ppm) is a very demanding task, especially in harsh environments where factors such as water vapor interference, limited energy resources, and restricted volume availability pose significant challenges [6]. Some, if not all, of these often lead to arduous process reusability, ultimately compromising the thermodynamic efficiency and overall energy performance of the process [7, 8]. In addition, the need for CO_2 removal extends beyond combating climate change; it is also critical in closed-loop environments, such as crew cabins during space exploration, where exposure to elevated CO_2 concentrations poses long-term health risks [9].

Different atmospheric CO_2 removal strategies—including terrestrial sequestration, bioenergy with carbon capture and storage, geological storage, and mineral carbonation—have been explored recently, with DAC using solid adsorbents emerging as a particularly promising approach [10-13]. This process allows energy requirements to be concentrated primarily in the adsorbent material regeneration step, unlike other approaches where entire stream heating, cooling, or compression are the most energy-intensive processes [13]. Among the most studied adsorbent materials are activated carbon (AC), solid-supported amines, alkali-based adsorbents, metal-organic frameworks (MOFs), and zeolites. Activated carbon is widely used for CO_2 capture due to its low cost,

high surface area, moisture resistance, and low energy requirements for regeneration. However, to effectively remove CO_2 from the atmosphere, stronger carbon-binding interactions are needed, and AC lacks the necessary binding strength at the concentrations relevant to DAC [14]. In contrast, solid-supported amines have demonstrated high CO_2 removal capacities while maintaining performance in the presence of water vapor and the potential for regeneration at temperatures near 100˚C [15, 16]. However, exposure to ambient oxygen leads to oxidative degradation, compromising their cyclic stability [2, 14]. This degradation is further accelerated during regeneration steps, typically performed via temperature-swing adsorption, which represents a major drawback for DAC applications where multiple adsorption–desorption cycles are essential for process feasibility [17]. Alkali-based adsorbents, despite being a mature technology for CO_2 capture, require high temperatures for regeneration, in some cases approaching 900˚C, which increases operational costs in DAC systems [2]. On the other hand, MOFs have recently gained attention as promising physisorption-based materials for low-concentration CO_2 capture, owing to their tunable structures, high surface areas, and adjustable pore volumes. Despite these advantages, MOFs often suffer from low stability and sensitivity to water vapor. Consequently, recent research efforts have focused on improving MOF resistance to humidity while enhancing CO_2 capacity [18, 19]. For example, defect engineering strategies in materials such as MOF-808 have been shown to enhance CO_2 adsorption by creating coordinatively unsaturated metal sites through targeted framework modifications [20]. In addition, synthesis routes to produce MOF-74 containing both Co and Ni, or only Zn, have been reported to improve CO_2 adsorption capacity [21, 22]. However, while structural modifications have improved performance, the regeneration energy has become comparable to that of chemisorption-based materials, potentially increasing the overall operational cost of DAC systems [6, 13, 23]. In comparison, zeolites have also been shown to be effective at industrial scales for capturing trace concentrations of CO_2. Their structural stability and well-established scalable synthesis make them attractive for DAC technologies [24]. However, like MOFs, their CO_2 adsorption capacity is significantly reduced under humid conditions.

In fixed beds used to separate CO_2 from humid environments, a common problem is the CO_2 "roll-up," in which this adsorbate molecule is displaced from the adsorbent by water due to significant interactions with the surface [25]. To mitigate the reduction in working capacity under wet conditions, desiccant guards are often used to protect zeolites or MOFs, but this adds extra complexity to the removal process [14, 26], increasing the overall process volume and regeneration costs. A promising strategy to achieve the CO_2 separation without the need for a moisture guard bed is the design and use of hierarchical composite adsorbents with tailored hydrophobicity. This is possible through a core–shell configuration achievable via confined-space synthesis techniques. Hierarchical composite materials are widely used in catalysts, batteries, and environmental remediation applications, such as electromagnetic field shielding [27-32]. Previously, we attempted to elucidate the *in situ* growth of the SAPO-34 crystalline phase within the meso- and macropores of commercial AC (Darco KB-G) with the incorporation of extra-framework Sr^{2+} via ion exchange [33]. This confined-space crystallization technique exploits the geometric constraints imposed by the matrix's pore structure, which governs crystal nucleation and orientation, as previously demonstrated for nanocrystals embedded within nanoporous frameworks [34, 35]. The hierarchical concept was inspired

by the work of Chen and coworkers on the growth of zeolites within mesoporous carbons to yield zeolites with imprinted mesoporosity after carbon template removal [36], in our case, without the eventual removal of the carbon. The approach highlights the benefits of using AC as the shell material, which acts as a moisture barrier and enables better interaction between the SAPO-34 active sites, Sr^{2+} ions, and CO_2 molecules. As a result, this composite not only mitigates the performance loss of SAPO-34 in the presence of humidity but also improves the overall CO_2 capture process by reducing energy consumption, an essential factor for the economic viability of energy-intensive technologies such as DAC.

The effective removal of CO_2 at trace concentrations also demands a narrow region for the enthalpy of adsorption where binding is strong enough for effective capture, yet weak enough for practical regeneration (i.e., strong physisorption) [7]. Accordingly, recent efforts in DAC adsorbent design have explored the incorporation of alkaline earth metal cations, such as Ba^{2+}, to enhance CO_2 affinity at low partial pressures [37, 38]. In this work, we present a hierarchical composite incorporating barium sites, referred to as Ba^{2+}-CSAPO-34. Previous studies on non-composite SAPO-34 have demonstrated that incorporating Ba^{2+} enhances CO_2 selectivity compared to Sr^{2+}-based counterparts, but effective incorporation has been challenging, requiring multiple exchanges [39]. Earlier composite syntheses employed more readily exchangeable cations (e.g., strontium), to avoid complications from inefficient exchange. However, the optimized two-step ion-exchange protocol developed in this study now enables efficient Ba^{2+} incorporation. The enhancement plausibly arises from the larger ionic radius of Ba^{2+} (1.34 Å) compared to Sr^{2+} (1.12 Å) [40, 41], which could enable Ba^{2+} to occupy energetically favorable sites within the SAPO-34 chabazite framework, particularly near the center of six-membered ring windows connecting adjacent cages. This strategic positioning would also maximize electrostatic interactions between the cation's polarizable charge and the permanent CO_2 quadrupole moment. The Ba^{2+} lower electronegativity (0.89, vs. 0.95 for Sr^{2+}) also enhances charge polarization, strengthening the electrostatic field experienced by approaching CO_2 molecules while maintaining weaker interactions with the more polar water molecules, effectively addressing critical challenges associated with CO_2 capture at low concentrations and helping to overcome one of the primary limitations of physisorption-based technologies [40, 42, 43]. The superior performance of barium-containing adsorbent materials relative to their strontium analogs is plausibly attributed to differences in cation electronegativity and ionic radii [44]. The hierarchical structure, resulting from the *in situ* growth of the SAPO-34 crystalline phase within activated carbon (AC), was confirmed in the present study through transmission electron microscopy coupled with energy-dispersive X-ray spectroscopy (TEM/EDS) and pore size distribution (PSD) analysis. Fast Fourier Transform (FFT) analysis was used in an attempt to understand the confined growth of SAPO in the composite. The overall chemical composition of the adsorbent was determined using inductively coupled plasma optical emission spectrometry (ICP-OES), while the surface chemical state of the cation was characterized via X-ray photoelectron spectroscopy (XPS). Additionally, fixed-bed adsorption tests using multicomponent gas mixtures were conducted to evaluate the material's performance under conditions that simulate both terrestrial and closed-loop environments. Furthermore, phenomenological simulations were performed in COMSOL Multiphysics to describe fixed-bed adsorption tests through coupled mass and energy

balances. Once the phenomenological model was validated against experimental data, it was employed to predict CO_2 uptake under more realistic process conditions, such as DAC and closed-loop environment applications.

Nomenclature		**Greek symbols**	
C	Gas concentration (ppm)	ρ	Density (g/cm^3)
D	Bed diameter (m or cm)	v	Total volumetric flow (cm^3/min)
ΔH_{ads}	Heat of Adsorption (kJ/mol)	**Subscripts**	
L	Bed length (m or cm)	b	Breakthrough
P	Pressure (atm)	B	Bulk
q	Gas adsorption amount (mmoles/cm^3)	e	Equilibrium
S	Adsorbent selectivity (dimensionless)	g	Gas
T	Temperature (K or ℃)	i	Inlet
t	Time (min)	s	Saturation
V	Adsorbent bed volume (cm^3)	t	Outlet
y	Molar fraction		

2. Methods

2.1.Reagents and Materials

Reagents for synthesis and ion-exchange procedures were obtained from Sigma-Aldrich, USA and used as received: orthophosphoric acid (85 wt.%), aluminum isopropoxide (98%), LUDOX AM-30 (30 wt.% SiO_2), tetraethylammonium hydroxide (40 wt.%), and barium chloride dihydrate (99%). For the hierarchical composite, a Darko-KB-G activated carbon (AC) was used. Deionized water employed in the synthesis and ion-exchange procedures was produced in-house. Ultra-high-purity grade gases for detemplation, thermogravimetric analysis, and adsorption tests were supplied by Linde-Praxair, USA.

2.2. Adsorbent Synthesis and Ion-Exchange

The crystalline material (Na^+-SAPO-34) and the hierarchical composite (Na^+-CSAPO-34) were synthesized via hydrothermal crystallization using tetraethylammonium hydroxide (TEAOH) as a structure-directing agent (SDA), following procedures previously reported by our group [33]. The optimal amount of AC was identified based on its pore volume and observations of homogenization issues during synthesis. It was found that about 7 g of AC per 30 mL of gel was the maximum required to maintain homogenization; exceeding this amount led to solid aggregation. The procedure also included mixing the solution for 2 hours at room temperature. TEAOH was removed from the frameworks in a tubular, temperature-controlled muffle furnace at 550 °C under nitrogen flow (100 mL/min) for 30 h. The detemplated materials (Na^+-SAPO-34 and Na^+-CSAPO-34) were subsequently modified by liquid-phase ion exchange with a barium(II)-containing salt, as described elsewhere [39]. The ion-exchange procedure was designed to achieve as complete cation replacement as possible and optimized through two sequential steps of 48 h, with salt renewal after each step to maintain a favorable concentration gradient between the

nanoporous materials and the salt solution. A schematic summary for the composite synthesis is shown in Fig. S1.

2.3. X-ray Powder Diffraction and Transmission Electron Microscopy

The crystallinity of the ion-exchanged materials was confirmed by X-ray powder diffraction (XRD). XRD patterns were recorded using a Rigaku ULTIMA III diffractometer equipped with a Cu Kα anode (λ = 1.5418 Å), operated at 40 kV and 44 mA. Data were collected in the 2θ range of 2°–40° with a step size of 0.02° and a scan rate of 1° min^{-1}. Particle morphology, elemental mapping, and structural features associated with SAPO-34 crystal growth within activated carbon were characterized using a high-resolution FEI Talos F200X Scanning/Transmission Electron Microscope (S/TEM) located at the Center for Functional Nanomaterials (CFN), Brookhaven National Laboratory, Upton, NY, USA. Samples were dispersed in 20 mL of anhydrous ethanol, sonicated for 5 min, and deposited onto ultrathin carbon films supported by lacey carbon on a 400-mesh copper grid.

d-Spacing values for the crystalline phase Ba^{2+}-SAPO-34 and the composite material Ba^{2+}-CSAPO-34 were determined using Fast Fourier Transform (FFT) analysis of TEM images. First, TEM images were visually inspected to identify regions showing parallel lattice fringes corresponding to a crystalline phase. Once these areas were identified, FFT patterns were obtained using ImageJ software [45]. From the resulting FFT images, the *d*-spacing values for each region were measured by analyzing the reciprocal lattice spacings in the FFT patterns. The calculated *d*-spacing values were then compared with those reported by the International Zeolite Association for a pure CHA rhombohedral sequence [46] from the crystal structure reported by Calligaris et al. [47].

2.4. Thermogravimetric Analysis (TGA) and Inductively Coupled Plasma Optical Emission Spectrometry (ICP-OES)

Thermal stability, optimal activation temperature prior to gas adsorption, and regeneration conditions were evaluated by thermogravimetric analysis (TGA). Profiles were obtained using a TA Q500 system under constant air or nitrogen flow (60 mL/min), heating samples from room temperature to 900 °C at 15 °C/min. Complementary analyses were performed using inductively coupled plasma optical emission spectrometry (ICP-OES) to determine overall chemical composition. ICP-OES measurements were carried out at Galbraith Laboratories, Inc. (Knoxville, TN, USA).

2.5. X-ray Photoelectron Spectroscopy (XPS)

Surface chemical states of ion-exchanged samples were probed by X-ray photoelectron spectroscopy (XPS) using a PHI VersaProbe II instrument with monochromatized Al Kα radiation (hv = 1486.6 eV). High-resolution XPS spectra were collected at a pass energy of 46.95 eV with 0.1 eV steps, calibrated to C 1s at 284.5 eV. Samples were degassed in situ overnight at room temperature prior to analysis.

2.6. Contact Angle Measurements

Contact angle measurements were performed to evaluate the hydrophobicity of the adsorbent materials. Measurements were obtained using a Krüss DSA-25B unit equipped with a high-resolution, high-speed camera.

2.7. Textural Properties and Equilibrium Adsorption Tests

Textural properties were determined from equilibrium nitrogen adsorption isotherms collected at -196°C (77K) using a Micromeritics ASAP 2020 volumetric adsorption instrument equipped with turbomolecular drag pumps for ultra-high vacuum conditions. For all adsorption equilibrium measurements reported in this work, sample holders were fitted with isolation valves to prevent exposure to the ambient during transfer. Prior to analysis, samples were degassed under high vacuum at 375 °C for 16 h. Micropore size distributions were estimated using the Horváth–Kawazoe method with the Chen–Yang correction, while mesopore sizes were derived using the Barrett–Joyner–Halenda (BJH) method [48, 49].

CO_2 and N_2 equilibrium adsorption isotherms were also measured at multiple temperatures near or above ambient and up to 1 atm, employing the Micromeritics ASAP 2020 and the same adsorbent pretreatment conditions stated above. Constant temperature was maintained using either a water bath or heating blankets. Water vapor adsorption equilibrium isotherms were obtained with an Anton Paar Autosorb 6100 volumetric adsorption unit. Prior to measurement, samples were degassed in situ at 350 °C for 16 h under vacuum. Water vapor adsorption isotherms were collected up to 90% relative humidity (RH), with heating blankets used to control temperature. CO_2 and H_2O isosteric heats of adsorption values were estimated using the Clausius–Clapeyron equation, applied to pure-component equilibrium adsorption isotherms measured at different temperatures

$$\left(\frac{d\ lnP}{d(1/T)}\right)_{q_e\ =\ constant} = -\frac{\Delta H_{ads}}{R} \qquad \text{Equation 1}$$

where P is the equilibrium pressure at q_e (equilibrium adsorption amount), T is the absolute temperature, and R is the gas constant. The three temperatures used for CO_2 measurements to estimate the isosteric heats of adsorption were 0, 25, and 50 °C. However, for H_2O vapor adsorption, only temperatures of 20 and 40 °C were used to ensure consistent temperature between the heating mantles and the sample cell. This prevents condensation in the cell. All of the adsorption isotherm data are presented in the Supplementary Information.

The corresponding adsorbed amounts were normalized by the volume of adsorbent rather than by weight to account for differences in the density of each composite's dominant phase.

2.8. Dynamic Adsorption Experiments and COMSOL Multiphysics Modeling

For fixed-bed tests, adsorbent materials were prepared as pellets to minimize pressure drop. A phenolic resin (GP 5520) and a water/polyvinyl acetate (PVA) mixture (3:1) were used as binders to form granules. In a typical preparation, 10 wt.% phenolic resin was combined with the adsorbent material, and a minimal amount of the water/PVA solution was added until a homogeneous mixture was obtained. The resulting paste was extruded using a punch-die unit at a compression load of 5000 lbf. The tablets were then dried and pyrolyzed at 550 °C under a constant nitrogen flow of 100 mL/min for 24 h.

Dynamic adsorption experiments were conducted in stainless steel columns with lengths of 7.62 and 16 cm, and an inner diameter of 0.3175 cm. Further details, including schematics, on the fixed-bed experimental setup and the adsorbent bed thermal treatment are available elsewhere [33]. Mass flow controllers used for precise flow

delivery control were calibrated prior to each fixed-bed experiment. The bed outlet concentration for CO_2 or H_2O was monitored using a Hiden Analytical QGA mass spectrometer with a detection limit of 100 ppb. The dynamic CO_2 adsorption capacity at any time, *t*, was calculated using a transient mass balance over the fixed-bed volume:

$$q = \frac{y_{CO_2}\rho_g v \rho_B}{MW_{CO_2} V_{bed}} \int_0^t \left(1 - \frac{c(t)}{c_i}\right) dt \qquad \text{Equation 2}$$

where q is the CO_2 adsorption amount (mmoles/cm^3; q_b and q_s at breakthrough and saturation, respectively) at time (t). The bed inlet CO_2 molar fraction is denoted by y_{CO_2}, v is the total volumetric flow (cm^3/min), ρ_g is the gas density (g/cm^3), ρ_B is the adsorbent material bulk density (g/cm^3); MW_g is the gas molecular weight, while V_{bed} is the adsorbent bed volume (cm^3). The transient outlet CO_2 concentration and the constant inlet concentration are represented by $c(t)$ and c_i, respectively. It is important to note that the reported adsorption capacities were normalized by the adsorbent volume rather than by mass to account for density differences among the composite phases.

Phenomenological modeling of dynamic adsorption experiments was performed using the COMSOL Multiphysics software suite and the Finite Element Method [50]. The model was intended to describe a 1-D transient adsorption process, accounting for dispersion, mass transfer resistance, and heat exchange throughout the bed. All the governing equations, boundary conditions, and initial conditions are presented in the Supplementary Information.

3. Results

3.1. Space-confined Synthesis and Characterization

A hierarchical composite named Na^+-CSAPO-34 was prepared via confined-space hydrothermal crystallization of SAPO-34 within the meso- and macro-pores of a Darco KG-B activated carbon (AC), using tetraethylammonium hydroxide (TEAOH) as a structure-directing agent (SDA) and following procedures previously reported by Hernández-Maldonado and co-workers, including observing homogenization [33]. After confirming the crystallinity and periodic phase of the hierarchical composite (Fig. 1A), the particle morphology and structural features associated with the growth of SAPO-34 crystalline phases within the AC matrix were carefully examined by transmission electron microscopy (TEM). TEM imaging of Ba^{2+}-SAPO-34 (Figs. 1B, 1C, and S2) revealed well-defined lattice planes, consistent with its expected CHA crystalline structure. In contrast, Ba^{2+}-CSAPO-34 exhibited a predominantly amorphous morphology, attributed to the confined-space nucleation within carbon and under which randomly oriented SAPO-34 crystalline domains are grown. The successful nucleation of SAPO-34 with a typical rhombohedral morphology (*a* = 9.459 Å and α = 94.07˚) [51] within the AC pores requires the critical nucleus size to fall within the meso- and macropore size range (i.e., <20 Å) [34]. Under these conditions, the crystal growth is more likely to occur at multiple sites within the meso- and macropores of the AC, leading to several randomly oriented crystals (Figs. 1B, 1C, and S2) [34].

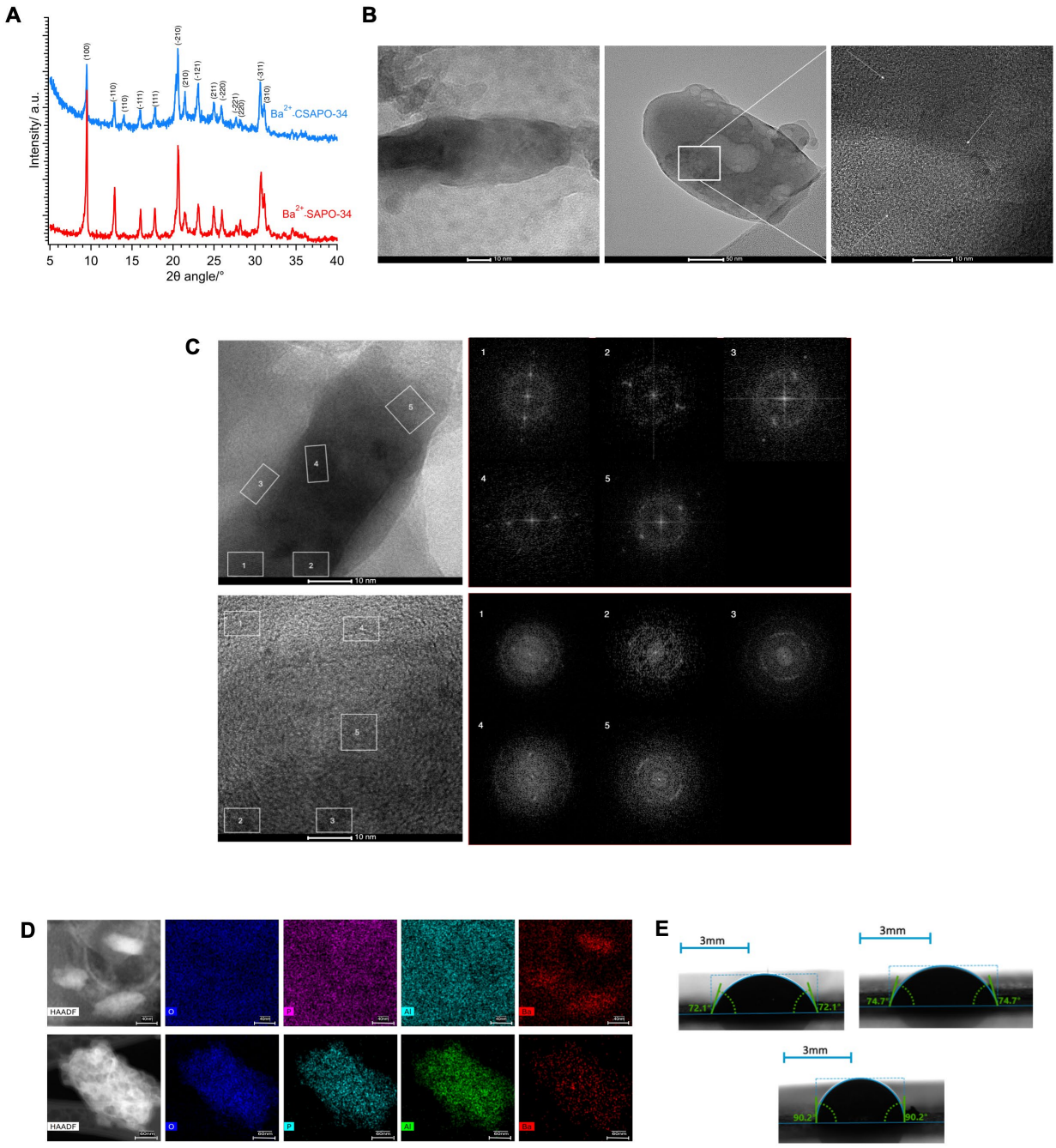

Fig. 1 Composite long-range order, structural and morphology information, and hydrophobicity level (A) X-ray diffraction patterns of ion-exchanged materials. **(B)** Transmission electron images for Ba^{2+}-SAPO-34 zeolite crystals *(left)* and Ba^{2+}-CSAPO-34 composite *(middle and right)*. **(C)** TEM images (left) that were employed for Fast Fourier Transform (FFT) of a higher magnification (right) to estimate *d*-spacing data in Ba^{2+}-SAPO-34 (top) and Ba^{2+}-CSAPO-34 (bottom). The depicted regions (5 each material) showed parallel lattice fringes indicative of crystalline phases. **(D)** Energy dispersive analysis by X-ray mapping for Ba^{2+}-SAPO-34 *(up)* and Ba^{2+}-CSAPO-34 *(bottom)*. **(E)** Contact angle measurements for Ba^{2+}-SAPO-34 *(left)*, Activated Carbon *(right)*, and Ba^{2+}-CSAPO-34 *(bottom)*.

Further structural analysis using Fast Fourier Transform (FFT) of higher-magnification TEM images enabled the estimation of *d*-spacing values (Fig. 1C and Table 1). Ba^{2+}-CSAPO-34 tends to exhibit smaller interplanar spacing compared to the purely crystalline phase. This is likely a consequence of the confined-space synthesis conditions within the AC matrix. The spatial constraints imposed by the AC pore network can restrict crystal growth and induce additional structural stress, thereby contributing to lattice contraction and reduced interplanar spacing [35, 52, 53].

Table 1. *d*-Spacing estimation using Fast Fourier Transform (FFT) of higher-magnification TEM images. The data are compared with those reported for a rhombohedral CHA sequence.

Ads. Material	**TEM Image Section / Fig. 1C**	***d*-Spacing Estimated (Å)** [+]	**Nearby *d*-Spacing as reported for a pure CHA phase (Å)** [++]	**Difference Δ*d* (Å)** (x 10^2)
Ba^{2+}-SAPO-34	4	2.2300	2.2269	0.31
	2	2.4444	2.3757	6.87
	5	2.8556	2.8564	-0.08
	1	3.1360	3.1359	0.01
	3	4.1000	4.0842	1.58
Ba^{2+}-CSAPO-34	1	1.91875	1.9198	-0.105
	3	2.1277	2.1319	-0.42
	4	2.2100	2.2269	-1.69
	5	3.1111	3.1359	-2.48
	2	3.6818	3.6172	6.46

[+] Estimated from FFT higher magnification from TEM images illustrated in **Fig. 1C**.
[++] *d*-spacing reported by Calligaris et al. for a rhombohedral CHA structure.

Additional evidence of the *in situ* formation of SAPO-34 within the AC void spaces was obtained through energy-dispersive X-ray spectroscopy (EDS) mapping, which revealed a uniform distribution of aluminum, phosphorus, oxygen, and extraframework barium throughout the composite (Fig. 1D and Table S1). The EDS mapping also quantitatively matched the results of an ICP-OES analysis (see Table S1); the latter were used to determine the crystal-phase unit-cell compositions (see Table 2). For the $Ba2^{+}$-CSAPO-34 material, the unit-cell composition is reported with NH_4^+ rather than H^+. As demonstrated in our previous work [33], the presence of the activated carbon (AC) shell provides thermal insulation to the SAPO-34 core, leading to reduced intracrystalline temperatures during thermal treatment. Under these conditions, partial decomposition of the organic structure-directing agent (TEA^+) results in the retention of NH_4^+ species within the SAPO-34 framework. The textural properties also shown in Table 2 were determined from nitrogen adsorption–desorption equilibrium isotherms collected at −196 °C (Fig. S3). Pore occupancy in the composite was determined by integrating the meso- and macropore regions of the pore size distribution (PSD) profiles (shown in Fig. S3), revealing that approximately 82% of the activated carbon void spaces were filled with SAPO-34 in the hierarchical composite. Moreover, the PSD profiles indicate that the activated carbon's intrinsic microporosity is largely preserved. This observation is consistent with the dimensions of the SAPO-34 unit cell (i.e., a = 9.459 Å and α = 94.07˚),

further indicating that *in situ* crystallization predominantly occurs within the meso- and macropores rather than within the microporous network.

One of the primary objectives of designing the hierarchical composite was to enhance the hydrophobicity of the Ba^{2+}-SAPO-34 crystalline phase by incorporating AC as a water-protecting shell. Thermogravimetric analysis (TGA) revealed a substantial reduction in water loss relative to the pure crystalline phase, decreasing from 14 wt.% in Ba^{2+}-SAPO-34 to 9 wt.% in the hierarchical composite (Fig. S4). The enhanced hydrophobic character composite is further supported by contact angle measurements (Fig. 1E) and dynamic breakthrough experiments, the results of which will be detailed in subsequent sections. Furthermore, thermogravimetric analysis (TGA) was used to determine the zeolite content, revealing that approximately 34 vol.% of the Ba^{2+}-SAPO-34 composite corresponds to the crystalline SAPO-34 phase

Table 2. Unit cell composition, textural properties, and heat of adsorption data for selected materials

Ads. Material	SAPO Phase Unit Cell	ρ_B‡ (g/cm³)	BET Surface Area (m^2/cm^3)	BJH Pore volume (cm^3/cm^3)	HK Pore volume (cm^3/cm^3)	Content of SAPO-34 Phase in Composite + (vol.%)	Occupancy of Carbon Meso- and Macro-pores by SAPO-34 + (%)	CO_2 Heat of Ads. (kJ/mol)±	H_2O Heat of Ads. (kJ/mol)±
AC	--	0.31	402	0.37	0.10	--	--	23.23	10.32
Ba^{2+}-SAPO-34	$Ba_{1.13}Na_{1.35}H_{2.48}[Si_{3.59}Al_{19.26}P_{13.16}O_{72}]$	0.81	205	--	0.16	--	--	42.08	59.06
Ba^{2+}-CSAPO-34	$Ba_{1.38}Na_{0.38}(NH_4)_{2.62}[Si_{2.98}Al_{19.39}P_{13.63}O_{72}]$	0.70	418	0.18	0.091	34	82	31.50	17.04
Ba^{2+}-SAPO-34/AC Physical Mixture	--	0.56	554	0.18	0.084	34	0	22.05	34.59

‡ρ_B is the adsorbent material bulk density.
± Reported values are averages calculated from isosteric heat of adsorption profiles (see Fig. 2).
+Values estimated from TGA and PSD data.

3.2. Pure Component Equilibrium Adsorption

The pure component gas adsorption properties of Ba^{2+}-CSAPO-34 were evaluated initially using volumetric equilibrium isotherms for CO_2, H_2O vapor (Fig. 2), N_2, and O_2 (Fig. S5). AC exhibits weak interactions with CO_2, whereas Ba^{2+}-SAPO-34 shows significantly stronger adsorption behavior. A physical mixture was prepared by mechanically combining the individual AC and SAPO-34 phases in the same weight fractions as those in Ba^{2+}-CSAPO-34. The adsorption isotherm of this physical mixture exhibited a linear superposition of the individual contributions from SAPO-34 and activated carbon, consistent with the independent behavior of each phase without synergistic interactions. However, in the hierarchical composite, the adsorption behavior is predominantly governed by the embedded SAPO-34.

Closer examination reveals that Ba^{2+}-exchanged materials exhibit stronger interactions with CO_2 compared to their Sr^{2+}-exchanged counterparts (Del Valle-Pérez et al. [33]). Specifically, Ba^{2+}-CSAPO-34 adsorbs 0.14 mmol/cm³ of CO_2, representing a 22% increase over the Sr^{2+}-CSAPO-34 material. The Sr^{2+}-CSAPO-34 analogue adsorbs about 0.29 mmol of CO_2 per gram of SAPO-34 within the composite at 10^{-3} atm, while the corresponding Ba^{2+}-CSAPO-34 composite adsorbs 0.38 mmol/g under the same conditions. When normalized by the SAPO-34 unit cell composition, this corresponds to roughly 0.8 CO_2 molecules per SAPO-34 unit cell for Sr^{2+}-CSAPO-34 and 1.0 CO_2

molecule per unit cell for Ba^{2+}-CSAPO-34. The enhanced interactions are attributed to the high quadrupole moment of CO_2 and its interaction with the electric field generated by the cations at the SAPO-34 surface (Table S2). Although both alkaline earth metals possess similar physical properties, as stated before, their CO_2 adsorption behaviors differ due to electronegativity; there is greater electron density localization on the Sr^{2+} cation and a correspondingly weaker polarizing electric field at the adsorption site. A reduced field strength would lead to somewhat weaker electrostatic interactions with the CO_2 quadrupole moment, resulting in slightly lower adsorption capacity. Additionally, the larger ionic radius of Ba^{2+} compared to Sr^{2+} (1.34 vs 1.13 Å) may promote the redistribution of residual Na^+ ions into hexagonal prism sites within the framework, thereby altering the surface electric potential distribution [54]. In contrast, Na^+ cations in the Sr^{2+}-exchanged materials may remain partially within the supercage, potentially diminishing the material's interaction with CO_2 [39].

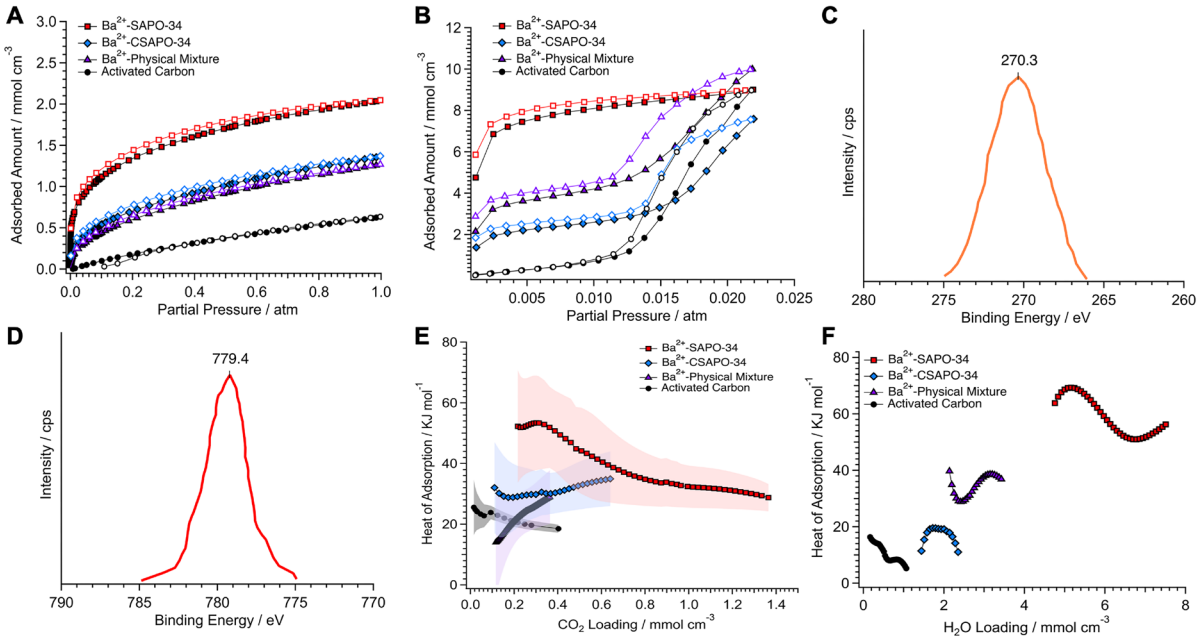

Fig. 2. Equilibrium adsorption performance, chemical states, and isosteric heat of adsorption profiles. **(A)** Carbon dioxide pure component equilibrium adsorption isotherm data gathered at 25°C. **(B)** Water vapor pure component equilibrium adsorption isotherm data gathered at 20°C. **(C)** High-resolution 3p XPS spectrum for strontium (II) ion-exchanged SAPO-34 surface. **(D)** High-resolution 3d XPS spectrum for barium (II) ion-exchanged SAPO-34 surface. **(E)** Isosteric heat of adsorption profiles of CO_2 for adsorbent materials, data include error shading. **(F)** Isosteric heat of adsorption profiles of H_2O vapor for adsorbent materials. General Notes: adsorption and desorption data depicted by closed and open markers, respectively. Loadings were normalized by volume of adsorbent instead of weight to consider differences in bulk density of each phase in the composite.

An attempt to further elucidate the electronic environment of the cations in SAPO was made via X-ray photoelectron spectroscopy (XPS). For comparison, a Sr^{2+} exchanged SAPO-34 sample was prepared here, and a peak at 270.3 eV was observed and assigned to Sr^{x+} ($3p_3/_2$) where *x*+ is the corresponding valence or charge (Fig. 2C). Literature

reports binding energies of 269.8 eV for Sr^0 ($3p_{3/2}$) and approximately 270.8 eV for Sr^{2+} ($3p_{3/2}$) [55], so the measured binding energy here indicates a partially reduced strontium species on the SAPO-34 surface, with an oxidation state lower than 2+, possibly due to electron donation from the zeolite framework and consistent with previous findings [56]. In contrast, a Ba^{2+}-SAPO-34 spectrum revealed a peak at 779.4 eV, corresponding to Ba^{x+} ($3d_{5/2}$) (Fig. 2D). This binding energy aligns with reported values for Ba^{2+} in BaO (779.1–779.8 eV) [57], strongly suggesting that barium retains its 2+ oxidation state on the SAPO-34 framework surface. Non-specific interactions, such as electrostatic repulsion and dispersion, are strongly influenced by the polarizability of the interacting species, in this case, Ba^{2+} and Sr^{2+} with CO_2. The polarizability of a cation depends on both its ionic radius and charge density. Therefore, given its larger ionic radius (lower charge density) and lower electronegativity, Ba^{2+} exhibits enhanced polarizability and thus stronger interactions with CO_2 molecules. Analogous analyses could be made with respect to other, specific interactions, such as ion-induced dipoles.

Regarding water vapor adsorption isotherms, distinct behaviors were observed for each material (Fig. 2B). Ba^{2+}-SAPO-34 exhibits a type I isotherm, characteristic of microporous solids, with sharp uptake at low relative pressure reflecting its strong hydrophilicity. In contrast, AC displays a type IV isotherm, indicative of weak water interactions and consistent with its low surface polarity relative to other commercial carbons [58]. For Ba^{2+}-CSAPO-34 composites, the isotherms combine features of types I and IV, suggesting that adsorption is governed by both the crystalline (core) and carbon (shell) phases (Fig. 2B). At low relative humidity, water adsorption is dominated by the SAPO-34 phase, while at higher humidity levels, the interaction strength with the zeolite decreases as water clustering occurs, and water molecules preferentially adsorb onto available oxygen-containing functional groups (carbonyl, hydroxyl, carboxyl) on the activated carbon surface [24]. Notably, the Ba^{2+}-CSAPO-34 composite shows an isotherm similar in shape to that of AC, but with reduced water uptake. This arises because many functional groups in the carbon phase interact with the SAPO-34 framework during synthesis, limiting their availability for water adsorption [33]. This also explains why Ba^{2+}-CSAPO-34 exhibits a higher water contact angle than AC (Fig. 1E), confirming enhanced hydrophobicity. Moreover, the composite shows minimal N_2 and O_2 adsorption at ambient temperature (Fig. S5), due to their significantly lower quadrupole moment compared to CO_2 (Table S2), further emphasizing its selectivity under practical operating conditions. For the Ba^{2+}-SAPO-34/AC physical mixture, the water vapor isotherm indicates the absence of a core-shell structure, with a profile that closely resembles the average sum of the individual adsorption isotherms of the phases.

The interactions between CO_2 and H_2O with the adsorbent materials were further quantified through isosteric heat of adsorption profiles (Fig. 2; corresponding adsorption data shown in Figs. S6 and S7). For CO_2, Ba^{2+}-SAPO-34 exhibits a heterogeneous surface profile, characterized by maximum interaction energies of approximately 55 kJ/mol (Fig. 2E). These high-energy sites are likely associated with CO_2 adsorption at Ba^{2+} cation sites within the framework, which are presumed to occupy preferred crystallographic positions, such as sites II′ and III. Once these sites are occupied by CO_2 molecules, the interaction energy decreases to approximately 35 kJ/mol, corresponding to adsorption on lower-energy sites, such as residual Na^+ sites. The average interaction

energy for CO_2 adsorption on Ba^{2+}-SAPO-34 was calculated to be 42.08 kJ/mol. In contrast, AC exhibits a homogeneous adsorption profile, with an average interaction energy of 23.23 kJ/mol. For the physical mixture (Ba^{2+}-Physical Mixture), a similar average interaction energy of 22.05 kJ/mol was observed, indicating that the phases do not interact synergistically. In Ba^{2+}-Physical Mixture, the presence of AC significantly influences the overall surface electrostatic potential, resulting in reduced adsorbate–adsorbent interactions compared to the hierarchical composite. In the Ba^{2+}-CSAPO-34 composite, however, the interaction energy is much higher (31.50 kJ/mol), demonstrating that CO_2 adsorption is primarily driven by the crystalline SAPO-34 phase rather than by the activated carbon phase.

For H_2O adsorption, the isosteric heat profiles reveal that Ba^{2+}-SAPO-34 exhibits strong interactions, with an average interaction energy of 59.06 kJ/mol (Fig. 2F). Activated carbon, as expected, shows much weaker interactions with an average interaction energy of 10.32 kJ/mol. In the physical mixture, higher interaction energies with water (34.59 kJ/mol) were obtained, reflecting the dominant influence of the hydrophilic SAPO-34 crystalline phase. Conversely, in the Ba^{2+}-CSAPO-34 composite, significantly lower interaction energies with water (17.04 kJ/mol) were recorded compared to CO_2, highlighting the hydrophobic character imparted by the activated carbon phase. This synergistic combination of both phases within the hierarchical structure effectively reduces water interactions while maintaining strong CO_2 binding, as corroborated by breakthrough experiments. Although Ba^{2+}-CSAPO-34 exhibits moderate interaction energies for both gases, they remain within the range typical of strong physisorption (30–60 kJ/mol). Further, as shown in Fig. S5, the adsorption–desorption isotherms for all tested adsorbates show reversibility.

3.3. Fixed Bed Studies

Competitive dynamic adsorption experiments with CO_2/N_2 and $CO_2/N_2/H_2O$ mixtures were conducted at representative feed CO_2 concentrations (500, 1000, and 2500 ppm) and ambient temperature. The fixed-bed apparatus and its operation are detailed in our previous work [33]. As expected under dry conditions (CO_2/N_2), the breakthrough curves of both adsorbents exhibit significant CO_2 adsorption (Fig. 3A), but the performance of Ba^{2+}-SAPO-34 is severely compromised in the presence of water vapor (Fig. 3B), a common limitation of many zeolitic materials [24]. Under humid, multicomponent conditions, the non-composite shows a clear CO_2 roll-up effect, which here means a temporary rise in outlet CO_2 levels above the inlet level caused by incoming water molecules displacing previously adsorbed CO_2, leading to a significant drop in working capacity (Fig. 3B and Table S4). But this is effectively mitigated by the Ba^{2+}-CSAPO-34 composite through its hydrophobic AC shell, providing a promising alternative for DAC, and for closed-loop systems where weight and volume constraints are critical. As shown in Figs. 3B and S9, no roll-up phenomenon is observed for Ba^{2+}-CSAPO-34 at any of the tested inlet CO_2 concentrations. Further, this material achieves CO_2 working capacities of 0.094, 0.115, and 0.153 mmol/cm³ for 500, 1000, and 2500 ppm CO_2, respectively, under a harsh 90% relative humidity (breakthrough curves shown in Figs. 3B and S9). From Fig. 3, it is clear that water breaks through much earlier than CO_2 in the hierarchical composite bed (Figs. 3B vs. 3D), providing further evidence of the composite's

hydrophobic nature, as H_2O easily accesses and passes through the structure, while CO_2 is mainly retained within the adsorption sites.

Given the CO_2 significant quadrupole moment and H_2O high dipole moment (Table S2), both molecules should strongly interact with cationic sites [33, 59, 60]. However, the absence of a roll-up effect in the composite breakthrough data is possibly attributed to the surface chemistry of the AC shell: hydrophobic carbons with minimal oxygen functionalization preferentially adsorb weakly polar CO_2 over strongly polar H_2O [61, 62]. In Ba^{2+}-CSAPO-34, the hydrophobic AC shell reduces overall water affinity while hindering water transport to the SAPO-34 core, preserving CO_2 access to high-affinity Ba^{2+} sites. This is supported by the isosteric heat data, showing significantly reduced H_2O binding (59.06 average for the pristine zeolite vs. 17.04 kJ/mol average for the composite) while maintaining adequate CO_2 binding in the composite (31.50 kJ/mol average). The AC used in this study, Darco KB-G, exhibits lower surface polarity than other commercial carbons, resulting in reduced affinity for polar molecules [58]. Water vapor equilibrium uptake (Fig. 2B) indicates that adsorption behavior in Ba^{2+}-CSAPO-34 is governed by contributions from both the carbon shell and the crystalline core. At low relative humidity, the crystalline Ba^{2+}-SAPO-34 phase dominates the adsorption process, evidenced by the Type I isotherm character and the minimal contribution from AC alone in this region. This phase contains extra-framework Ba^{2+} cations that act as primary adsorption sites through strong electrostatic interactions [33]. At higher relative humidity, the composite adsorbs increasing amounts of water, exhibiting behavior characteristic of the hydrophobic AC component. This increase is attributed to capillary condensation within the hierarchical pore structure of the AC shell, driven by water–water hydrogen bonding [61, 62]. Previous studies have shown that under such conditions, water molecules form hydrogen-bonded clusters that preferentially nucleate at functional groups on the carbon surface [24]. These clusters can vary in size depending on humidity, with effective radii ranging from 3.85 Å (small oligomers) to 19.85 Å (large aggregates), and exhibit significantly reduced mobility compared to individual CO_2 molecules [63]. Given that the eight-membered ring pore aperture of Ba^{2+}-SAPO-34 is approximately 4–5 Å, only individual water molecules and the smallest water clusters would penetrate the SAPO-34 micropores [56, 63]. Once inside, water competes directly with CO_2 molecules for the Ba^{2+} cation sites, thereby causing the roll-up behavior observed in Ba^{2+}-SAPO-34 breakthrough data under humid conditions.

In contrast, the Ba^{2+}-CSAPO-34 composite, with its core–shell architecture, provides additional adsorption volume within the hierarchical meso- and macropore network of the activated carbon shell. Structural characterization reveals that approximately 20% of the composite's meso-/macro-pore volume remains unoccupied by the crystalline phase; therefore, it could effectively sequester larger water clusters before they reach the SAPO-34 core, and this would be equivalent to approximately 4.11 mmol of water per cm^3 of composite, assuming that the adsorbed phase density there is close to that of the liquid state. From Fig. 2B, a desorption hysteresis due to capillary condensation is observed in the composite, occurring within the meso- and macro-pores and corresponding to approximately 4.07 mmol of water adsorbed per cm^3, remarkably close to the estimated capacity based on the available void spaces in the composite. The hierarchical nature of the composite framework, combined with the hydrophobic character of the AC surface

and the kinetic hindrance to water diffusion through the tortuous porous network, likely protects the Ba^{2+} active sites and maintains CO_2 capture performance even under high humidity conditions. Further, the binding energy between water molecules and typical oxygen-containing functional groups on carbons (e.g., carboxyl, hydroxyl), as estimated from ab initio calculations, is relatively low (~40 kJ/mol), whereas, compared with previously reported CO_2 binding energy on another alkaline earth (Sr^{2+}) adsorption site (125 kJ/mol) [39, 64, 65]. This differential binding affinity explains the absence of roll-up behavior in Ba^{2+}-CSAPO-34: the material provides two spatially segregated adsorption environments, Ba^{2+} cation sites within the SAPO-34 framework for selective CO_2 capture and hydrophobic voids in the AC shell for water sequestration.

Comparing Ba^{2+}-CSAPO-34 with the previously reported Sr^{2+}-CSAPO-34 hierarchical composite [33] under humid CO_2 capture conditions, the Ba^{2+} analogue exhibits 74.5, 4.35, and 14.4% higher removal efficiencies at inlet concentrations of 500, 1000, and 2500 ppm CO_2, respectively. This nonlinear performance improvement indicates that CO_2 adsorption at these concentrations involves distinct adsorption regimes associated with different types of adsorption sites. At low CO_2 concentrations (500 ppm), adsorption is dominated by the highest-energy sites and is mainly driven by electrostatic interactions between CO_2 molecules and extra-framework cations. In this regime, Ba^{2+}-CSAPO-34 clearly outperforms the Sr^{2+} analogue due to the larger ionic radius and greater polarizability of Ba^{2+}, which generate a stronger local electrostatic field and thus a higher affinity for CO_2. As the inlet CO_2 concentration increases, these high-energy sites become quickly saturated, and adsorption progressively occurs on lower-energy sites. In this higher-concentration range, both materials show similar accessibility to adsorption sites, as indicated by their comparable microporous pore volumes (Ba^{2+}-CSAPO-34: 0.091 cm^3 cm^{-3}; Sr^{2+}-CSAPO-34: 0.11 cm^3 cm^{-3}). Consequently, their adsorption capacities become similar, and the relative performance advantage of Ba^{2+} incorporation diminishes. Overall, these findings suggest that Ba^{2+} incorporation mainly improves CO_2 affinity rather than increasing the total number of available adsorption sites. Therefore, the most significant performance gains occur at ultra-low CO_2 concentrations, while at higher concentrations, both materials exhibit similar capacities, with Ba^{2+}-CSAPO-34 consistently maintaining a modest performance edge.

To further assess the performance of Ba^{2+}-CSAPO-34, experiments were conducted at varying flow rates and bed lengths to determine optimal operating conditions. At a fixed flow rate of 200 mL/min and CO_2 representative concentration of 1000 ppm under humid conditions (RH = 90%), two bed depths (7.62 and 16 cm) were evaluated using the same column diameter (D = 0.3175 cm). Table S5 and Fig. S10 show that increasing bed depth by nearly 50% results in only a 16% increase in processed bed volumes (from 2,503 to 2,983), indicating the development of a somewhat extended mass transfer zone. Moreover, greater bed depths correlate with improved fractional bed utilization and higher capacities, suggesting a possible reduction in diffusion limitations. Subsequently, three different flow rates were tested using the deeper bed to evaluate flow rate effects. As shown in Fig. S10, lower flow rates (i.e., longer residence times) slightly improve adsorption capacity, confirming that intraparticle mass transfer is the rate-controlling step.

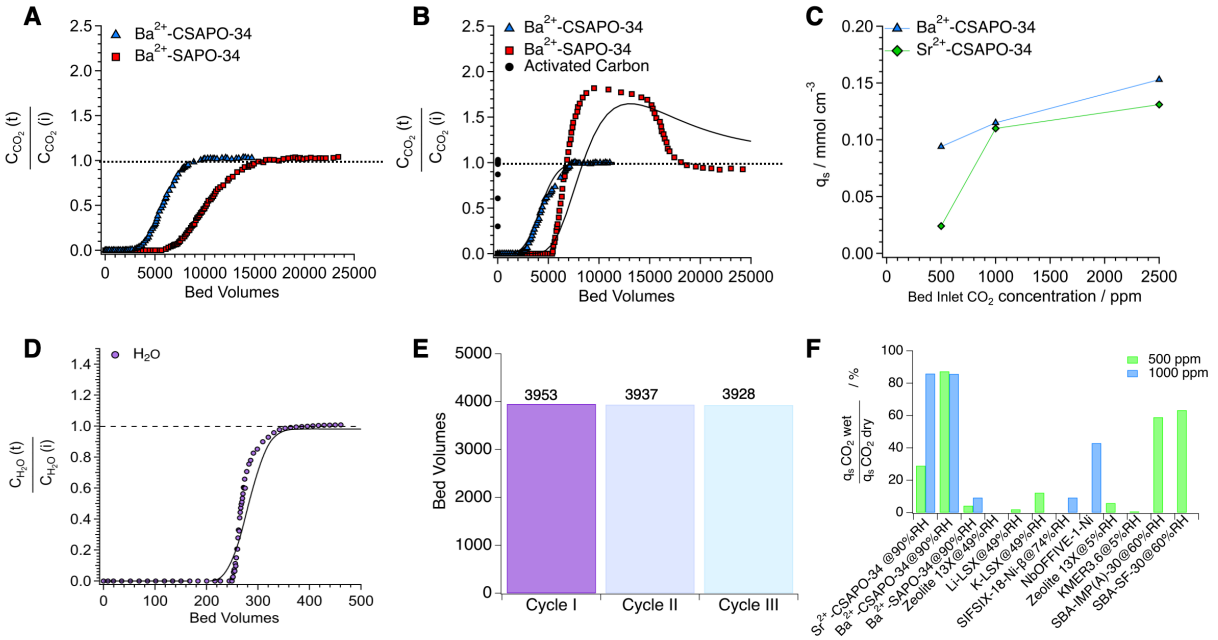

Fig. 3. Fixed bed adsorption performance, recyclability, and phenomenological modeling. **(A)** CO_2 breakthrough curves under dry nitrogen. **(B)** CO_2 breakthrough curves under humid nitrogen, inlet RH of 90%. **(C)** CO_2 fixed bed saturation loading amounts at 25°C as a function of inlet concentrations (Sr^{2+}-CSAPO data from Del Valle et al. [33]) **(D)** H_2O breakthrough curves under humid nitrogen, inlet RH 90% and 500 ppm inlet CO_2. **(E)** Recyclability assessment for Ba^{2+}-CSAPO-34 fixed beds and a CO_2 feed concentration of 500 ppm using humid nitrogen (RH = 90 %) as a carrier gas. **(F)** Comparison of humid versus dry media treatment capacities for several reported adsorbent materials at CO_2 concentrations near 500 and 1000 ppm (see Table S6). General notes: (i) CO_2 fixed-bed data were gathered for C_i = 500 ppm, L = 7.62 cm, and ν = 200 mL/min; (ii) detection limit in CO_2 or H_2O fixed bed outlet concentration measurements was 100 ppb; (iii) for thermal recyclability assessment, the bed was regenerated at 175 °C and vacuum conditions ($1.1x10^{-3}\ torr$).

A critical aspect in the context of DAC and closed-loop environments is the regeneration of the adsorbent, as this step is among the most energy-intensive [12, 13]. The recyclability of Ba^{2+}-CSAPO-34 was evaluated through fixed-bed CO_2 breakthrough experiments and, as shown in Fig. 3E, the material retained its adsorption capacity over three cycles, after *in situ* regeneration by thermal treatment at 175 °C for 16 h under vacuum ($1.1\text{x}10^{-3}$ torr). Figure 3F also compares Ba^{2+}-CSAPO-34 capacity at humid conditions relative to dry conditions with that of previously reported adsorbents, all for low-concentration CO_2 removal [18, 19, 24, 33, 66, 67]. The results demonstrate that Ba^{2+}-CSAPO-34 maintains its adsorption capacity from dry to humid environments, with a capacity approximately 79% larger than other zeolites, such as faujasite (FAU) (see Table S6). Further, compared against the previously reported Sr^{2+}-CSAPO-34 composite, Ba^{2+}-CSAPO-34 exhibits a 74% larger capacity at 500 ppm CO_2 and 4% higher capacity at 1000 ppm CO_2, highlighting the advantage of Ba^{2+} as an adsorption site over Sr^{2+}. Compared with hydrophobic MOFs, Ba^{2+}-CSAPO-34 also exhibits an adsorption capacity approximately 19% higher. It is worth noting, however, that while certain modified MOFs can adsorb considerable amounts of CO_2 under humid conditions, they

often exhibit roll-up and moisture-induced polymorphic phase transitions [18, 19]. These effects complicate regeneration and lead to higher energy consumption during CO_2 removal. In contrast, Ba^{2+}-CSAPO-34 maintains stable adsorption behavior without roll-up, offering improved operational robustness.

Relative to functionalized mesoporous silica (SBA) adsorbents, Ba^{2+}-CSAPO-34 retains a larger fraction of its CO_2 uptake capacity under humid conditions, indicating superior moisture tolerance. Materials that exhibit enhanced CO_2 uptake in the presence of humidity are predominantly chemical adsorbents, most notably amine-functionalized sorbents, in which water directly participates in the chemisorption mechanism. Despite their high capacities, amine-based adsorbents suffer from well-known limitations, including oxidative degradation in the presence of oxygen, urea formation under CO_2-rich conditions, steam-induced degradation of the support matrix, and irreversible adsorption of acidic contaminants such as SO_2 [14, 17]. These degradation pathways compromise cyclic stability and pose significant challenges for DAC applications that require several adsorption–desorption cycles. Additionally, the potential release of volatile or toxic degradation products raises concerns for deployment in closed-loop or life-support environments [24]. Overall, Ba^{2+}-CSAPO-34 represents a complementary adsorption strategy that prioritizes humidity tolerance, structural stability, and relatively low-energy regenerability under realistic operating conditions, even though water does not directly enhance its CO_2 adsorption capacity.

3.4. Phenomenological Modeling and Process Scaling

A mathematical model of a fixed-bed adsorber was used to describe the adsorption dynamics, through mass and energy balances, enabling correlation of the experimentally obtained results with the underlying adsorption mechanisms under realistic operating conditions. Since the adsorption process considered here is a purification step (e.g., trace CO_2 capture), the pressure drop was assumed to be negligible because the fluid velocity does not change significantly. This assumption is valid for gas stream mixtures that contain trace amounts of adsorbates and when the adsorption of the carrier gas is negligible in comparison, which is the case here (Fig.S5). The mass and energy balances, along with the parameters for the one-dimensional, axially dispersed plug-flow model (see Supplementary Information), were simulated in COMSOL [50]. Figs. 3B, 3D, and S9 show the experimental breakthrough curves obtained for Ba^{2+}-CSAPO-34 and Ba^{2+}-SAPO-34 under humid conditions, along with the theoretical breakthrough curves estimated from the phenomenological model. In general, the model predictions describe the experimental data well. However, within the mass transfer zone (MTZ) and at the end of the breakthrough, the model tends to deviate from the experimental curves. This may be attributed to a decrease in the adsorption rate in that region, as the bed approaches saturation; consequently, the overall mass transfer coefficient is expected to decrease over time [68]. Nevertheless, this effect cannot be captured in the simulation because a constant mass transfer coefficient (K_g) was assumed in the Linear Driving Force (LDF) approximation used in the modeling. In the case of the Ba^{2+}-SAPO-34 breakthrough profiles, this deviation is more pronounced, which might be due to roll-up behavior.

Further, the LDF model assumes the adsorbent consists of homogeneous particles, where diffusion occurs with constant effective diffusivity, and the adsorbed amount within the pores rapidly reaches equilibrium [68]. Although this assumption generally holds, it

may not be entirely valid for shorter breakthrough times. However, Table S7 shows that the model predicts well the bed volumes and saturation capacities at the breakthrough points for the hierarchical composite. Additionally, the predictive model captured thermal effects due to the adsorption (Fig. S11), showing that the temperature increase during the adsorption step is negligible (<1 K).

The performance of a fixed-bed experiment is governed by the combined effect of selectivity and uptake capacity [69]. One of the most widely used methods to estimate the selectivity of an adsorbent under multicomponent mixtures is the Ideal Adsorbed Solution Theory (IAST) [69]. However, various studies have shown that IAST tends to fail in cases where strong bonding occurs between adsorbates or when segregation effects are present, meaning that adsorbates preferentially occupy specific sites within the adsorbent [70, 71] . Based on this and considering the nature of our separation system (N_2, CO_2, H_2O), IAST calculations may not be appropriate to estimate selectivity in our process. Nevertheless, phenomenological modeling provides a suitable approach for estimating the selectivity of the adsorbents toward CO_2. Experimental water fixed-bed adsorption data (Fig. 3D) were gathered and compared with the phenomenological model, which described the breakthrough behavior well. Based on the modeling results for different CO_2 inlet concentrations, CO_2 selectivity values were estimated (Table 3). As observed, the Ba^{2+}-CSAPO-34 adsorbent material exhibits significant selectivity toward CO_2 even in the presence of humidity, with a selectivity of up to 51.56. Compared with the single-crystalline, non-composite Ba^{2+}-SAPO-34 phase, the hydrophobic activated carbon phase incorporated into the composite improves both selectivity and CO_2 uptake capacity.

It should be noted that the development of this phenomenological model and its ability to accurately predict the fixed-bed adsorption behavior of Ba^{2+}-CSAPO-34 provide a foundation for scalability assessments under realistic process conditions. Currently, DAC has been under increasing scrutiny, particularly concerning the adsorbents employed in these systems [72]. Climeworks is recognized as one of the leading industrial key players in atmospheric CO_2 removal. Based on the adsorbent plate geometry described in its patents, a scalability assessment of the adsorption process employing Ba^{2+}-CSAPO-34 was performed (see Table S8 for the simulation parameters) [73, 74]. The analysis relied on a set of simplifying assumptions related to the contactor design and operating conditions. In particular, the physical dimensions of the adsorption module, including bed length and void fraction, were selected as representative values to enable comparison across different systems. An average superficial air velocity of 0.028 m s^{-1} was assumed, consistent with values reported in the literature and chosen to ensure a low pressure drop across the sorbent layers [73]. Based on the analysis, Ba^{2+}-CSAPO-34 could remove about 5.4 kt of CO_2 annually, assuming 281 daily cycles of operation. This exceeds the performance of other tested solid adsorbents for this purpose [6, 75] and is comparable to Climeworks' ORCA facility, which is reported to remove around 4 kt of CO_2 per year [12]. One of the main concerns when employing solid adsorbents for DAC processes is their reduced performance under humid conditions, as water vapor in the atmosphere can limit their adsorption capacity. Ba^{2+}-CSAPO-34 addresses this issue, demonstrating CO_2 selectivity at low concentrations (~500 ppm) and maintaining its adsorption capacity in the presence of water vapor. Moreover, a scalability assessment of CO_2 removal in a closed-loop environment, such as the International Space Station, indicates that, based

on model predictions, Ba^{2+}-CSAPO-34 can remove approximately 5.1 kg of CO_2 per day at a partial pressure of 0.0025 atm, meeting the closed-loop environment demand (ca. 4.16 kg of CO_2 per day). Furthermore, at CO_2 partial pressure of 0.001 atm, this composite can remove 2.0 kg of CO_2 per day—almost twice the amount captured by currently used commercial adsorbent materials [76, 77].

Table 3. Summary of capacity and selectivity data as estimated from phenomenological modeling.

Ads. Material	CO_2 conc. (ppm)	Adsorbate	Bed Volumes*	q_s (mmol/cm³)¥	CO_2/H_2O Selectivity
Ba^{2+}-SAPO-34	500	CO_2	5,400	0.0148	0.114
		H_2O	2,191	7.31	
	1000	CO_2	4,536	0.0283	0.218
		H_2O	2,096	7.31	
	2500	CO_2	1,990	0.145	1.12
		H_2O	2,001	7.30	
Ba^{2+}-CSAPO-34	500	CO_2	2,125	0.0863	15.52
		H_2O	229	0.3136	
	1000	CO_2	1,853	0.118	25.90
		H_2O	184	0.257	
	2500	CO_2	1,126	0.181	51.56
		H_2O	141	0.198	

*Estimated at breakthrough point, $\frac{C_t}{C_i} > 0$.

¥ Estimated at breakthrough saturation, , $\frac{C_t}{C_i} = 1$.

4. Conclusions

A hierarchical composite was successfully synthesized via a confined-space hydrothermal crystallization strategy, in which the meso- and macroporous network of activated carbon (AC) guides nucleation and growth of SAPO-34. TEM analysis confirmed that SAPO-34 crystalline nucleate randomly within the internal pore structure of the AC, while FFT analysis revealed a reduced *d*-spacing, consistent with confinement-induced lattice compression. Incorporating Ba^{2+} cations into the SAPO-34 framework was shown to selectively improve CO_2 adsorption by strengthening electrostatic interactions and enhancing the polarizability of the adsorption sites, especially at low CO_2 partial pressures relevant to DAC and closed-loop environments. At the same time, the hierarchical composite architecture weakens water–adsorbent interactions compared to the pure crystalline phase, as evidenced by hydrophobic surface behavior and stable adsorption performance under humid conditions. This decoupling of CO_2 affinity from water uptake offers a significant advantage over many humidity-assisted or chemisorptive systems. Dynamic fixed-bed adsorption experiments further demonstrated that Ba^{2+}-CSAPO-34 maintains high CO_2 selectivity (up to ~51.56 at 2500 ppm CO_2) in the presence of water vapor, exhibits sharp breakthrough fronts, and avoids roll-up effects

typically associated with competitive adsorption. Importantly, the material can be fully regenerated under mild conditions (175 °C and vacuum conditions), confirming its suitability for cyclic operation and energy-efficient deployment. To bridge experimental observations with practical implementation, a phenomenological fixed-bed adsorption model incorporating mass and energy balances was developed and validated against breakthrough data. The model accurately captured adsorption dynamics, saturation behavior, and competitive effects under realistic operating conditions, providing a reliable predictive framework for performance assessment beyond equilibrium isotherms.

Overall, the combined effects of confined crystallization, Ba^{2+}-induced enhancement of CO_2 affinity, and hydrophobic buffering by the carbon matrix enable Ba^{2+}-CSAPO-34 to outperform various current zeolites and MOFs with hydrophobic characteristics. The results show that hierarchical zeolitic–carbon composites are a promising and scalable platform for selective CO_2 capture from moist gas streams, especially in applications where regenerability, stability, and volumetric efficiency are important.

Acknowledgements

This work was supported by the US National Aeronautics and Space Administration (NASA) the NASA MIRO-Puerto Rico Space Partnership for Research, Education, and Training (PRSPRInT) grant no. 80NSSC19M0236. The TEM work at BNL was made possible through a collaboration supported by the National Science Foundation (NSF) grant DMR- 2425113. This research used the Electron Microscopy facilities of the Center for Functional Nanomaterials (CFN), which is a U.S. Department of Energy Office of Science User Facility, at Brookhaven National Laboratory under Contract No. DE-SC0012704. We also acknowledge the support from Puerto Rico NASA Space Grant Consortium Graduate Fellowships Program under grant no. 80NSSC20M0052.

CRediT authorship contribution statement

A.J.H.-M. conceived and supervised the project. **G.C.D.-P.** synthesized and characterized the materials, set up and conducted all the adsorption tests, and conducted all the mathematical modeling. **J.C.M.-S.** helped with the confined-space synthesis routines. **K.K.** performed the TEM tests. **S.E.-S.** and **E.M.-R.** helped with the fixed-bed adsorption runs. **G.C.D.-P.** and **A.J.H.-M.** wrote the initial draft of the manuscript. All the authors discussed the results and revised the manuscript.

Competing Interests

The authors declare no competing interests.

Additional Information

Supplementary information is available.

Data Availability

Data will be made available on request.

References

[1] P. Friedlingstein, M. O'Sullivan, M. Jones, R. Andrew, J. Hauck, P. Landschützer, C. Le Quéré, H. Li, I. Luijkx, A. Olsen, G. Peters, W. Peters, J. Pongratz, C.

Schwingshackl, S. Sitch, J. Canadell, P. Ciais, R. Jackson, S. Alin, A. Arneth, V. Arora, N. Bates, M. Becker, N. Bellouin, C. Berghoff, H. Bittig, L. Bopp, P. Cadule, K. Campbell, M. Chamberlain, N. Chandra, F. Chevallier, L. Chini, T. Colligan, J. Decayeux, L. Djeutchouang, X. Dou, C. Rojas, K. Enyo, W. Evans, A. Fay, R. Feely, D. Ford, A. Foster, T. Gasser, M. Gehlen, T. Gkritzalis, G. Grassi, L. Gregor, N. Gruber, Ö. Gürses, I. Harris, M. Hefner, J. Heinke, G. Hurtt, Y. Iida, T. Ilyina, A. Jacobson, A. Jain, T. Jarníková, A. Jersild, F. Jiang, Z. Jin, E. Kato, R. Keeling, K. Goldewijk, J. Knauer, J. Korsbakken, X. Lan, S. Lauvset, N. Lefèvre, Z. Liu, J. Liu, L. Ma, S. Maksyutov, G. Marland, N. Mayot, P. McGuire, N. Metzl, N. Monacci, E. Morgan, S. Nakaoka, C. Neill, Y. Niwa, T. Nützel, L. Olivier, T. Ono, P. Palmer, D. Pierrot, Z. Qin, L. Resplandy, A. Roobaert, T. Rosan, C. Rödenbeck, J. Schwinger, T. Smallman, S. Smith, R. Sospedra-Alfonso, T. Steinhoff, Q. Sun, A. Sutton, R. Séférian, S. Takao, H. Tatebe, H. Tian, B. Tilbrook, O. Torres, E. Tourigny, H. Tsujino, F. Tubiello, G. van der Werf, R. Wanninkhof, X. Wang, D. Yang, X. Yang, Z. Yu, W. Yuan, X. Yue, S. Zaehle, N. Zeng, J. Zeng, Global Carbon Budget 2024, ESSD 17(3) (2025) 965–1039. https://doi.org/10.5194/essd-17-965-2025

[2] D. Fu, M.E. Davis, Carbon dioxide capture with zeotype materials, Chem. Soc. Rev. 51(22) (2022) 9340–9370. https://doi.org/10.1039/D2CS00508E

[3] Y. Qiu, P. Lamers, V. Daioglou, N. McQueen, H.-S. de Boer, M. Harmsen, J. Wilcox, A. Bardow, S. Suh, Environmental trade-offs of direct air capture technologies in climate change mitigation toward 2100, Nat. Commun. 13(1) (2022) 3635. https://doi.org/10.1038/s41467-022-31146-1

[4] S. Chowdhury, Y. Kumar, S. Shrivastava, S.K. Patel, J.S. Sangwai, A Review on the Recent Scientific and Commercial Progress on the Direct Air Capture Technology to Manage Atmospheric CO_2 Concentrations and Future Perspectives, Energy Fuels 37(15) (2023) 10733–10757. https://doi.org/10.1021/acs.energyfuels.2c03971

[5] Y. Chen, R. Wu, P.-C. Hsu, Perspective on distributed direct air capture: what, why, and how?, npj Mater. Sustain. 3(1) (2025) 12. https://doi.org/10.1038/s44296-025-00056-w

[6] A. Sodiq, Y. Abdullatif, B. Aissa, A. Ostovar, N. Nassar, M. El-Naas, A. Amhamed, A review on progress made in direct air capture of CO_2, Environ. Technol. Innov.. 29 (2023) 102991. https://doi.org/10.1016/j.eti.2022.102991

[7] T.M. Nisbet, A.W. van der Made, Direct air capture of CO_2: an industrial perspective, Curr. Opin. Chem. Eng. 50 (2025) 101190. https://doi.org/10.1016/j.coche.2025.101190

[8] R. Surkatti, Y.M. Abdullatif, R. Muhammad, A. Sodiq, K. Mroue, T. Al-Ansari, A.I. Amhamed, Comparative analysis of amine-functionalized silica for direct air capture (DAC): Material characterization, performance, and thermodynamic efficiency, Sep. Purif. Technol. 354 (2025) 128641. https://doi.org/10.1016/j.seppur.2024.128641

[9] M.R. Georgescu, A. Meslem, I. Nastase, Accumulation and spatial distribution of CO_2 in the astronaut's crew quarters on the International Space Station, Build. Environ. 185 (2020) 107278. https://doi.org/10.1016/j.buildenv.2020.107278

[10] M. van der Spek, A. Bardow, C.M. Baum, V. Bolongaro, V. Dufour-Décieux, C. Esch, L. Fritz, S. Garcia, C. Hamann, D. Hondeborg, A. Kiani, S. Lueck, S.K. Patel, S.B. Peh, M. Pisciotta, P. Psarras, T. Repke, P.A. Sáenz-Cavazos, I. Schulte, D. Shu, Q. Shu, B. Sovacool, J. Strefler, S.V. Castaño, J.-Y. Wang, M. Wessling, J. Wilcox, J. Young, J.C. Minx, An ecosystem of carbon dioxide removal reviews – part 1: direct air CO_2 capture and storage, Energy Environ. Sci. 18(22) (2025) 9713–9785. https://doi.org/10.1039/D5EE01732G

[11] C. Chuah, Y. Ho, A. Syed, K. Thivyalakshmi, E. Yang, K. Johari, Y. Yang, W. Poon, Applicability of Adsorbents in Direct Air Capture (DAC): Recent Progress and Future Perspectives, Ind. Eng. Chem. Res. 64(8) (2025) 4117–4147. https://doi.org/10.1021/acs.iecr.4c03265

[12] M. Ozkan, S.P. Nayak, A.D. Ruiz, W. Jiang, Current status and pillars of direct air capture technologies, iScience 25(4) (2022) 103990. https://doi.org/10.1016/j.isci.2022.103990

[13] M. Erans, E.S. Sanz-Pérez, D.P. Hanak, Z. Clulow, D.M. Reiner, G.A. Mutch, Direct air capture: process technology, techno-economic and socio-political challenges, Energy Environ. Sci. 15(4) (2022) 1360–1405. https://doi.org/10.1039/D1EE03523A

[14] L. Jiang, W. Liu, R.Q. Wang, A. Gonzalez-Diaz, M.F. Rojas-Michaga, S. Michailos, M. Pourkashanian, X.J. Zhang, C. Font-Palma, Sorption direct air capture with CO_2 utilization, Prog. Energy Combust. Sci. 95 (2023) 101069. https://doi.org/10.1016/j.pecs.2022.101069

[15] J. Elfving, J. Kauppinen, M. Jegoroff, V. Ruuskanen, L. Järvinen, T. Sainio, Experimental comparison of regeneration methods for CO2 concentration from air using amine-based adsorbent, Chem. Eng. J. 404 (2021) 126337. https://doi.org/10.1016/j.cej.2020.126337

[16] K. An, K. Li, C.-M. Yang, J. Brechtl, K. Nawaz, A comprehensive review on regeneration strategies for direct air capture, J. CO2 Util. 76 (2023) 102587. https://doi.org/10.1016/j.jcou.2023.102587

[17] K. Min, W. Choi, C. Kim, M. Choi, Oxidation-stable amine-containing adsorbents for carbon dioxide capture, Nat. Commun. 9(1) (2018) 726. https://doi.org/10.1038/s41467-018-03123-0

[18] P.M. Bhatt, Y. Belmabkhout, A. Cadiau, K. Adil, O. Shekhah, A. Shkurenko, L.J. Barbour, M. Eddaoudi, A Fine-Tuned Fluorinated MOF Addresses the Needs for Trace CO_2 Removal and Air Capture Using Physisorption, J. Am. Chem. Soc. 138(29) (2016) 9301–7. https://doi.org/10.1021/jacs.6b05345

[19] S. Mukherjee, N. Sikdar, D. O'Nolan, D.M. Franz, V. Gascón, A. Kumar, N. Kumar, H.S. Scott, D.G. Madden, P.E. Kruger, B. Space, M.J. Zaworotko, Trace CO_2 capture by an ultramicroporous physisorbent with low water affinity, Sci. Adv. 5(11) (2019) eaax9171. https://doi.org/doi:10.1126/sciadv.aax9171

[20] A. Kazemi, M.A. Pordsari, M. Tamtaji, M.H. Afshari, S. Keshavarz, F. Zeinali, H. Baesmat, S. Zahiri, F. Manteghi, A. Ghaemi, S. Rohani, W.A. Goddard, Unveiling the power of defect engineering in MOF-808 to enhance efficient carbon dioxide adsorption and separation by harnessing the potential of DFT analysis, Chem. Eng. J. 494 (2024) 153049. https://doi.org/10.1016/j.cej.2024.153049

[21] A. Kazemi, M.A. Pordsari, M. Tamtaji, F. Manteghi, A. Ghaemi, S. Rohani, W.A. Goddard, Environmentally friendly synthesis and morphology engineering of mixed-metal MOF for outstanding CO_2 capture efficiency, Chem. Eng. J. 505 (2025) 158951. https://doi.org/10.1016/j.cej.2024.158951
[22] A. Kazemi, M.A. Pordsari, M. Tamtaji, F. Zainali, S. Keshavarz, H. Baesmat, F. Manteghi, A. Ghaemi, S. Rohani, W.A. Goddard Iii, Eco-Friendly Synthesis and Morphology Control of MOF-74 for Exceptional CO2 Capture Performance with DFT Validation, Sep. Purif. Technol. 361 (2025) 131328. https://doi.org/10.1016/j.seppur.2024.131328
[23] N. McQueen, K.V. Gomes, C. McCormick, K. Blumanthal, M. Pisciotta, J. Wilcox, A review of direct air capture (DAC): scaling up commercial technologies and innovating for the future, Prog. Energy 3(3) (2021) 032001. https://doi.org/10.1088/2516-1083/abf1ce
[24] J.M. Kolle, M. Fayaz, A. Sayari, Understanding the Effect of Water on CO_2 Adsorption, Chem. Rev. 121(13) (2021) 7280–7345. https://doi.org/10.1021/acs.chemrev.0c00762
[25] R.L. Siegelman, E.J. Kim, J.R. Long, Porous materials for carbon dioxide separations, Nat. Mater. 20(8) (2021) 1060–1072. https://doi.org/10.1038/s41563-021-01054-8
[26] G.E. Cmarik, J.C. Knox, Co-Adsorption of Carbon Dioxide on Zeolite 13X in the Presence of Preloaded Water, 48th International Conference on Environmental Systems Albuquerque, New Mexico, 2018, pp. ICES–2018–3.
[27] G. Cai, P. Yan, L. Zhang, H.-C. Zhou, H.-L. Jiang, Metal–Organic Framework-Based Hierarchically Porous Materials: Synthesis and Applications, Chem. Rev. 121(20) (2021) 12278–12326. https://doi.org/10.1021/acs.chemrev.1c00243
[28] B. Wen, H. Yang, Y. Lin, L. Ma, Y. Qiu, F. Hu, Y. Zheng, Synthesis of core–shell Co@S-doped carbon@ mesoporous N-doped carbon nanosheets with a hierarchically porous structure for strong electromagnetic wave absorption, J. Mater. Chem. A 9(6) (2021) 3567–3575. https://doi.org/10.1039/D0TA09393A
[29] K. Li, J. Yang, J. Gu, Hierarchically Porous MOFs Synthesized by Soft-Template Strategies, Acc. Chem. Res. 55(16) (2022) 2235–2247. https://doi.org/10.1021/acs.accounts.2c00262
[30] Y. Liu, Z. Chen, Z. Li, N. Zhao, Y. Xie, Y. Du, J. Xuan, D. Xiong, J. Zhou, L. Cai, Y. Yang, CoNi nanoalloy-Co-N4 composite active sites embedded in hierarchical porous carbon as bi-functional catalysts for flexible Zn-air battery, Nano Energy 99 (2022) 107325. https://doi.org/10.1016/j.nanoen.2022.107325
[31] L. Huang, J. Yang, Y. Zhao, H. Miyata, M. Han, Q. Shuai, Y. Yamauchi, Monolithic Covalent Organic Frameworks with Hierarchical Architecture: Attractive Platform for Contaminant Remediation, Chem. Mater. 35(7) (2023) 2661–2682. https://doi.org/10.1021/acs.chemmater.2c03282
[32] R. Jia, R. Zhang, L. Yu, X. Kong, S. Bao, M. Tu, X. Liu, B. Xu, Engineering a hierarchical carbon supported magnetite nanoparticles composite from metal organic framework and graphene oxide for lithium-ion storage, J. Colloid Interface Sci. 630 (2023) 86–98. https://doi.org/10.1016/j.jcis.2022.10.088
[33] G.C. del Valle-Pérez, J.C. Muñoz-Senmache, P.E. Cruz-Tato, E. Nicolau, A.J. Hernández-Maldonado, Carbon Dioxide Removal from Humid Atmosphere by a

Porous Hierarchical Silicoaluminophosphate/Carbon Composite Adsorbent, ACS Appl. Eng. Mater. 1(2) (2023) 790–801. https://doi.org/10.1021/acsaenm.2c00208
[34] H. Bishara, S. Berger, Preferred crystallographic orientation of nanocrystals embedded inside nanopores, Prog. Cryst. Growth Charact. Mater. 65(4) (2019) 100464. https://doi.org/10.1016/j.pcrysgrow.2019.100464
[35] F.C. Meldrum, C. O'Shaughnessy, Crystallization in Confinement, Adv. Mater. 32(31) (2020) e2001068. https://doi.org/10.1002/adma.202001068
[36] H.Y. Chen, J. Wydra, X.Y. Zhang, P.S. Lee, Z.P. Wang, W. Fan, M. Tsapatsis, Hydrothermal Synthesis of Zeolites with Three-Dimensionally Ordered Mesoporous-Imprinted Structure, Journal of the American Chemical Society 133(32) (2011) 12390–12393. https://doi.org/10.1021/ja2046815
[37] D.Y. Kim, K.-H. Ryu, W.B. Bae, H. Min, S. Kweon, M.B. Park, D. Kang, Y.J. Kim, S.B. Kang, Active metal cation exchanged in ZSM-5 for enhanced direct air capture of CO_2, Chem. Eng. J. 503 (2025) 158380. https://doi.org/10.1016/j.cej.2024.158380
[38] J. Moral-Pombo, E. García-Bordejé, Y. Liu, A. Guerrero-Ruiz, I. Rodríguez-Ramos, CO_2 capture from air and its conversion to CH_4 using dual functional materials supported on high surface area graphite, J. CO2 Util. 93 (2025) 103054. https://doi.org/10.1016/j.jcou.2025.103054
[39] A.G. Arévalo-Hidalgo, J.A. Santana, R. Fu, Y. Ishikawa, A.J. Hernández-Maldonado, Separation of CO_2 from light gas mixtures using nanoporous silicoaluminophosphate sorbents: Effect of multiple-step ion exchange and adsorption mechanism via computational studies, Microporous Mesoporous Mater. 130(1-3) (2010) 142–153. https://doi.org/10.1016/j.micromeso.2009.10.025
[40] A. Itadani, A. Oda, H. Torigoe, T. Ohkubo, M. Sato, H. Kobayashi, Y. Kuroda, Material Exhibiting Efficient CO_2 Adsorption at Room Temperature for Concentrations Lower Than 1000 ppm: Elucidation of the State of Barium Ion Exchanged in an MFI-Type Zeolite, ACS Appl. Mater. Interfaces 8(13) (2016) 8821–8833. https://doi.org/10.1021/acsami.6b00909
[41] M. Fischer, R. Bell, Cation-exchanged SAPO-34 for adsorption-based hydrocarbon separations: predictions from dispersion-corrected DFT calculations, Physical Chemistry Chemical Physics 16(39) (2014) 21062–21072. https://doi.org/10.1039/c4cp01049c
[42] D. Boer, J. Langerak, P. Pescarmona, Zeolites as Selective Adsorbents for CO_2 Separation, ACS Appl. Energy Mater. 6(5) (2023) 2634–2656. https://doi.org/10.1021/acsaem.2c03605
[43] S. Lee, H. Lee, H. Hwang, D. Seoung, H. Kim, P. Kim, Y. Lee, Relationship Between Electronegativity of the Extra-Framework Cations and Adsorption Capacity for CO2 Gas on Mordenite Framework, Inorg. Chem. 64(2) (2025) 903–910. https://doi.org/10.1021/acs.inorgchem.4c04062
[44] V.R.C.M. Barbalho, P.V.S. Badolato, C. Detoni, M.M.V.M. Souza, CO_2 adsorption in 13X zeolite modified by alkaline earth cation exchange, Microporous Mesoporous Mater. 398 (2025) 113806. https://doi.org/10.1016/j.micromeso.2025.113806

[45] C.A. Schneider, W.S. Rasband, K.W. Eliceiri, NIH Image to ImageJ: 25 years of image analysis, Nat. Methods 9(7) (2012) 671–675. https://doi.org/10.1038/nmeth.2089
[46] L.B.M. Christian Baerlocher, Darren Brouwer, Bernd Marler, Database of Zeolite Structures. https://www.iza-structure.org/databases/.
[47] M. Calligaris, G. Nardin, L. Randaccio, Cation site location in hydrated chabazites. Crystal structure of potassium- and silver- exchanged chabazites, Zeolites 3(3) (1983) 205–208. https://doi.org/10.1016/0144-2449(83)90008-8
[48] E.P. Barrett, L.G. Joyner, P.P. Halenda, The determination of pore volume and area Distributions in porous substances. I. Computations from nitrogen isotherms, Journal of the American Chemical Society 73(1) (1951) 373–380. https://doi.org/10.1021/ja01145a126
[49] S.U. Rege, R.T. Yang, Corrected Horváth-Kawazoe equations for pore-size distribution, AIChE J. 46(4) (2000) 734–750. https://doi.org/https://doi.org/10.1002/aic.690460408
[50] COMSOL Multiphysics® v.6.2, COMSOL, Inc., 2025.
[51] E. Aghaei, M. Haghighi, Enhancement of catalytic lifetime of nanostructured SAPO-34 in conversion of biomethanol to light olefins, Microporous Mesoporous Mater. 196 (2014) 179–190. https://doi.org/10.1016/j.micromeso.2014.05.011
[52] Y.-S. Jun, Y. Zhu, Y. Wang, D. Ghim, X. Wu, D. Kim, H. Jung, Classical and Nonclassical Nucleation and Growth Mechanisms for Nanoparticle Formation, Annu. Rev. Phys. Chem. 73(Volume 73, 2022) (2022) 453–477. https://doi.org/10.1146/annurev-physchem-082720-100947
[53] A. F.M. Santos, M. Teresa Viciosa, I. Matos, J.C. Sotomayor, J.L. Figueirinhas, M.H. Godinho, L.C. Branco, C.J. Dias, M. Dionísio, Impact of nanoconfinement on the physical state and conductivity mechanisms of a 2-picolinium ionic liquid crystal, J. Mol. Liq. 403 (2024) 124830. https://doi.org/10.1016/j.molliq.2024.124830
[54] M. Fischer, R.G. Bell, Cation-exchanged SAPO-34 for adsorption-based hydrocarbon separations: predictions from dispersion-corrected DFT calculations, Physical Chemistry Chemical Physics 16(39) (2014) 21062–21072. https://doi.org/10.1039/C4CP01049C
[55] H. Van Doveren, J.A.T.H. Verhoeven, XPS spectra of Ca, Sr, Ba and their oxides, J. Electron. Spectrosc. Relat. Phenom. 21(3) (1980) 265–273. https://doi.org/10.1016/0368-2048(80)85055-9
[56] L. Zhang, M.E. Rivera-Ramos, A.J. Hernández-Maldonado, Location and valence state of strontium cations on the framework of a carbon dioxide selective porous silicoaluminophosphate, Chem. Eng. J. 209 (2012) 356–361. https://doi.org/10.1016/j.cej.2012.07.134
[57] J.F.S. Moulder, W. F.; Sobol, P. E, Handbook of X-ray Photoelectron Spectroscopy: A Reference Book of Standard Spectra for Identification and Interpretation of XPS data, Physical Electronics, Inc. 1992
[58] M.A. Martín-González, O. González-Díaz, P. Susial, J. Araña, J.A. Herrera-Melián, J.M. Doña-Rodríguez, J. Pérez-Peña, Reuse of Phoenix canariensis palm frond mulch as biosorbent and as precursor of activated carbons for the

adsorption of Imazalil in aqueous phase, Chem. Eng. J. 245 (2014) 348–358. https://doi.org/10.1016/j.cej.2014.02.050
[59] A. Rajendran, G.K.H. Shimizu, T.K. Woo, The Challenge of Water Competition in Physical Adsorption of CO_2 by Porous Solids for Carbon Capture Applications – A Short Perspective, Adv. Mater. 36(12) (2024) 2301730. https://doi.org/10.1002/adma.202301730
[60] A. Kumar, D.G. Madden, M. Lusi, K.J. Chen, E.A. Daniels, T. Curtin, J.J.t. Perry, M.J. Zaworotko, Direct Air Capture of CO2 by Physisorbent Materials, Angew. Chem. Int. Ed. Engl. 54(48) (2015) 14372–7. https://doi.org/10.1002/anie.201506952
[61] I.I. Salame, T.J. Bandosz, Study of Water Adsorption on Activated Carbons with Different Degrees of Surface Oxidation, J. Colloid Interface Sci. 210(2) (1999) 367–374. https://doi.org/10.1006/jcis.1998.5918
[62] L. Liu, S. Jin, Y. Park, Y.C. Park, C.-H. Lee, Sorption Equilibria and Kinetics of CO2, N2, and H2O on KOH-Treated Activated Carbon, Ind. Eng. Chem. Res. 57(50) (2018) 17218–17225. https://doi.org/10.1021/acs.iecr.8b03862
[63] Y. Gao, H. Fang, K. Ni, Y. Feng, Water clusters and density fluctuations in liquid water based on extended hierarchical clustering methods, Scientific Reports 12(1) (2022) 8036. https://doi.org/10.1038/s41598-022-11947-6
[64] L. Liu, S. Tan, T. Horikawa, D.D. Do, D. Nicholson, J. Liu, Water adsorption on carbon - A review, Adv. Colloid Interface Sci. 250 (2017) 64–78. https://doi.org/10.1016/j.cis.2017.10.002
[65] B. Collignon, P. Hoang, S. Picaud, J. Rayez, Ab initio study of the water adsorption on hydroxylated graphite surfaces, Chem. Phys. Lett. 406(4-6) (2005) 430–435. https://doi.org/10.1016/j.cplett.2005.03.026
[66] A.N. Stuckert, R.T. Yang, CO_2 capture from the atmosphere and simultaneous concentration using zeolites and amine-grafted SBA-15, Environ. Sci. Technol. 45(23) (2011) 10257–64. https://doi.org/10.1021/es202647a
[67] G.E. Decker, E.D. Bloch, Using Helium Pycnometry to Study the Apparent Densities of Metal-Organic Frameworks, ACS Appl. Mater. Interfaces 13(44) (2021) 51925–51932. https://doi.org/10.1021/acsami.1c07304
[68] F.J. Gutiérrez Ortiz, M. Barragán Rodríguez, R.T. Yang, Modeling of fixed-bed columns for gas physical adsorption, Chem. Eng. J. 378 (2019) 121985. https://doi.org/10.1016/j.cej.2019.121985
[69] R. Krishna, Screening metal–organic frameworks for mixture separations in fixed-bed adsorbers using a combined selectivity/capacity metric, RSC Adv. 7(57) (2017) 35724–35737. https://doi.org/10.1039/C7RA07363A
[70] J.J. Gutiérrez-Sevillano, S. Calero, R. Krishna, Selective Adsorption of Water from Mixtures with 1-Alcohols by Exploitation of Molecular Packing Effects in CuBTC, J. Phys. Chem. C 119(7) (2015) 3658–3666. https://doi.org/10.1021/jp512853w
[71] R. Krishna, J.M. van Baten, Segregation effects in adsorption of CO2-containing mixtures and their consequences for separation selectivities in cage-type zeolites, Sep. Purif. Technol. 61(3) (2008) 414–423. https://doi.org/10.1016/j.seppur.2007.12.003

[72] T. Fan, S. Shen, C.Y. Sit, P.J.A. Kenis, A. Chapman, Environmental, economic and social trade-offs of membrane-based direct air capture technologies integrated with CO_2 conversion using life cycle assessment, J. CO2 Util. 91 (2025) 103002. https://doi.org/10.1016/j.jcou.2024.103002
[73] C. Gebald, N. Piatkowski, T. Ruesch, J.A. Wurzbacher, Low-Pressure Drop Structure of Particle Adsorbent Bed for Adsorption Gas Separation Process., 2014.
[74] F. Sabatino, A. Grimm, F. Gallucci, M. van Sint Annaland, G.J. Kramer, M. Gazzani, A comparative energy and costs assessment and optimization for direct air capture technologies, Joule 5(8) (2021) 2047–2076. https://doi.org/10.1016/j.joule.2021.05.023
[75] G. Leonzio, P.S. Fennell, N. Shah, A Comparative Study of Different Sorbents in the Context of Direct Air Capture (DAC): Evaluation of Key Performance Indicators and Comparisons, Appl. Sci. 12(5) (2022) 2618. https://doi.org/10.3390/app12052618
[76] J.C. Knox, A.D. Ebner, M.D. LeVan, R.F. Coker, J.A. Ritter, Limitations of Breakthrough Curve Analysis in Fixed-Bed Adsorption, Ind. Eng. Chem. Res. 55(16) (2016) 4734–4748 https://doi.org/10.1021/acs.iecr.6b00516
[77] W.T. Peters, J.C. Knox, 4BMS-X Design and Test Activation, 47th International Conference on Environmental Systems, Charleston, SC, 2017, pp. ICES–2017–240.

Supplementary Information for

Adsorption-Based Direct Air Capture Using Hierarchical Porous Composites Prepared via Confined-Space Crystallization

Gabriela C. del Valle-Pérez[1], Juan Carlos Muñoz-Senmache[1], Sebastián Espiña-Santiago[1], Erick M. Mendez-Rios[1], Kim Kisslinger[2], and Arturo J. Hernández-Maldonado[1*]

[1]Department of Chemical Engineering, University of Puerto Rico Mayagüez Campus, Mayagüez, Puerto Rico 00680, USA

[2] Center for Functional Nanomaterials, Brookhaven National Laboratory, Upton, NY 11973

* To whom correspondence should be addressed. Email: arturoj.hernandez@upr.edu

The PDF file includes:

Phenomenological Modeling
Figs. S1 to S11
Tables S1 to S8
References

COMSOL Multiphysics Modeling

Mass and energy balance equations, along with kinetic rate expressions, were employed to describe the 1-D adsorption process, accounting for dispersion, mass transfer resistance, and heat exchange throughout the bed. Given the bed dimensions used, the gas velocity along the fixed bed was assumed to remain constant; therefore, the pressure drop across the column was considered negligible. The model assumes that: (i) the gas flow follows an axially dispersed plug-flow regime, (ii) the mass transfer rate can be represented by a Linear Driving Force (LDF) approximation, (iii) the gas phase behaves as an ideal mixture, and (iv) radial concentration gradients are negligible. Accordingly, the mass balance for each component, assuming the bed is adsorbate-free prior to each adsorption step, is given by Equation (S1), with the boundary and initial conditions defined by Equations (S2) and (S3), respectively.

$$-D_L \frac{\partial^2 y_i}{\partial z^2} + \frac{\partial y_i}{\partial t} + u \frac{\partial y_i}{\partial z} + y_i \frac{\partial u}{\partial z} + \frac{RT}{P}\left(\frac{1-\varepsilon_{bed}}{\varepsilon_{bed}}\right) \times \rho_s \frac{\partial q_i}{\partial t} = 0 \qquad \text{Equation S1}$$

$$z = 0 \qquad y\,(i,0) = y_{feed,i}$$

$$z = L \qquad \frac{\partial y(i,L)}{\partial z} = 0 \qquad \text{Equation S2}$$

$$y_i\,(0,z) = 0$$

$$q_i\,(0,z) = 0 \qquad \text{Equation S3}$$

Here, u is the gas superficial velocity, y_i is the gas-phase mole fraction of component i, q_i is the adsorbed amount, R is the gas constant, P is the total pressure, T_f is the gas temperature, ε_{bed} is the bed void fraction, and D_L is the axial dispersion coefficient. The mass transfer rate was represented by the LDF model (Equation S4):

$$\frac{\partial q_i}{\partial t} = K_G(q_i^* - q_i) \qquad \text{Equation S4}$$

Where q_i^* is the equilibrium adsorption capacity of component i, and K_G is the overall mass transfer coefficient. Equilibrium adsorption data were estimated using the Extended Langmuir isotherm model (Equation S5), which accounts for the contribution of each adsorbate during the multicomponent adsorption process:

$$q_i^* = q_{sat,i} \frac{K_{L,i} P_i}{1 + \sum_{i=1}^{n} K_{L,i} P_i} \qquad \text{Equation S5}$$

where $q_{sat,i}$ is the saturation adsorption capacity, $K_{L,i}$ is the Langmuir constant, and P_i is the partial pressure of component i. The temperature dependence of $K_{L,i}$ was determined using the Van't Hoff relation (Equation S6), assuming the average isosteric heat of adsorption ($\Delta H_{ads,avg.}$) from the profiles data:

$$\frac{dLnK_L}{dT_f} = -\frac{\Delta H_{ads,avg}}{RT_f^2}$$ Equation S6

Water vapor adsorption isotherms for the hierarchical composite Ba^{2+}-CSAPO-34 were fitted by dividing the data into multiple regions to achieve an optimal correlation. The model parameters were estimated using empirical correlations. The axial dispersion coefficient (D_L) was calculated using the Wakao–Funazkri correlation [1], and the overall mass transfer coefficient (K_G) where R_p is the radius of the particle [2], as expressed in Equations S7 and S8. The effective diffusivity (D_e) was estimated from Equation (S9), where ε is the particle void fraction and τ is the tortuosity factor. Molecular diffusivity (D_m) was estimated using the Chapman-Enskog kinetic theory [3].

$$D_L = \frac{D_m}{\varepsilon}(20 + \frac{1}{2}ScRe)$$ Equation S7

$$K_G = \frac{15D_e}{(R_p)^2}$$ Equation S8

$$D_e = \frac{\varepsilon}{\tau}(\frac{D_s D_m}{D_s + D_m})$$ Equation S9

Diffusion in the solid phases (D_s) was measured from fractional uptake data for each adsorbate. These were collected volumetrically using the Micrometrics ASAP 2020 for CO_2 and Anton Paar Autosorb 6100 for H_2O at ambient temperature under differential pressures of approximately 0.0005 atm (CO_2) and 0.018 atm (H_2O). The phenomenological volumetric transport model illustrated below was employed to evaluate the diffusional behavior of adsorbates in the hierarchical composite. The model assumed a finite gas volume system and spherical-shaped adsorbent particles [4]:

$$F = \frac{q(t)}{q_e} = 1 - \sum_{n=1}^{\infty} \frac{6\alpha(\alpha+1)}{9 + 9\alpha + q_n^2\alpha^2} \exp\left[-\frac{D_S q_n^2 t}{a^2}\right]$$ Equation S10

where ***F*** is the fractional uptake, ***q*** is the transient volumetric adsorption amount, q_e is the volumetric equilibrium adsorption amount, q_n***'s*** are the non-zero root values of $\tan q_n = 3q_n/(3 + \alpha q_n^2)$ and α is a parameter that can be expressed in terms of the final fractional uptake, (D_S a^{-2}) is the diffusion time constant (s^{-1}), ***t*** is time, and ***a*** is the characteristic length (particle effective radius).

For the energy balance, a pseudo-homogeneous model (Equation S11) was applied, assuming instantaneous thermal equilibrium between the gas and solid phases. Thus, a single energy balance was employed for the bed temperature. The energy balance for the column wall is described by Equation (S12), with boundary and initial conditions given in Equations (S13-14).

$$\left(\varepsilon\rho_f C_{p,f} + (1-\varepsilon)\rho_s C_{p,s}\right)\frac{\partial T_f}{\partial t} + \varepsilon\rho_f C_{\rho,f}\frac{\partial (uT_f}{\partial z} = k_{f,e}\frac{\partial^2 T_f}{\partial z^2} + (1-\varepsilon)\sum\left(-\Delta H_{ads,i}\right)\rho_s\frac{\partial q_i}{\partial t} - 4\frac{h_{in}}{D_{in}}(T_f - T_w) \quad \text{Equation S11}$$

$$\left(\rho_w C_{p,w}\, A_w\right)\frac{\partial T_w}{\partial t} = \pi D_{in} h_{in}\left(T_f - T_w\right) - \pi D_{out} h_{out}(T_w - T_0) \quad \text{Equation S12}$$

$$z = 0 \qquad T_f = T_0 \quad (t > 0)$$

$$z = L \qquad \frac{\partial T_f}{\partial z} = 0 \quad (t > 0) \quad \text{Equation S13}$$

$$T_f = T_{initial} \quad (0 \le z \le L) \quad \text{Equation S14}$$

The wall heat transfer coefficient (h_{in}) was estimated using the Li and Finlayson correlation for 1D models (Equation S15) [5], while the effective axial thermal conductivity ($k_{f,e}$) was estimated using the Yagi–Kunii–Wakao correlation modified by Krupiczka (Equation S16) [6, 7]. For natural convection, an external heat transfer coefficient of 5 $\frac{W}{m^2 K}$ between the bed and ambient air was assumed.

$$Nu_{in} = \frac{h_{in} D}{k_f} = 2.03 Re^{0.8} \exp\left(-\frac{6 d_p}{D}\right) \quad \text{Equation S15}$$

$$k_{f,e} = k_f\left(\left(\frac{k_s}{k_f}\right)^{0.28 - 0.757 log_{10}\left(\frac{k_s}{k_f}\right)} + 0.75 RePr\right) \quad \text{Equation S16}$$

On the other hand, to elucidate the adsorbent selectivity from the models, Equation (S17) was employed, where q denotes the adsorbed amount of each component, and P represents its partial pressure.

$$S_{CO_2/H_2O} = \frac{\frac{q_{CO_2}}{P_{CO_2}}}{\frac{q_{H_2O}}{P_{H_2O}}} \quad \text{Equation S17}$$

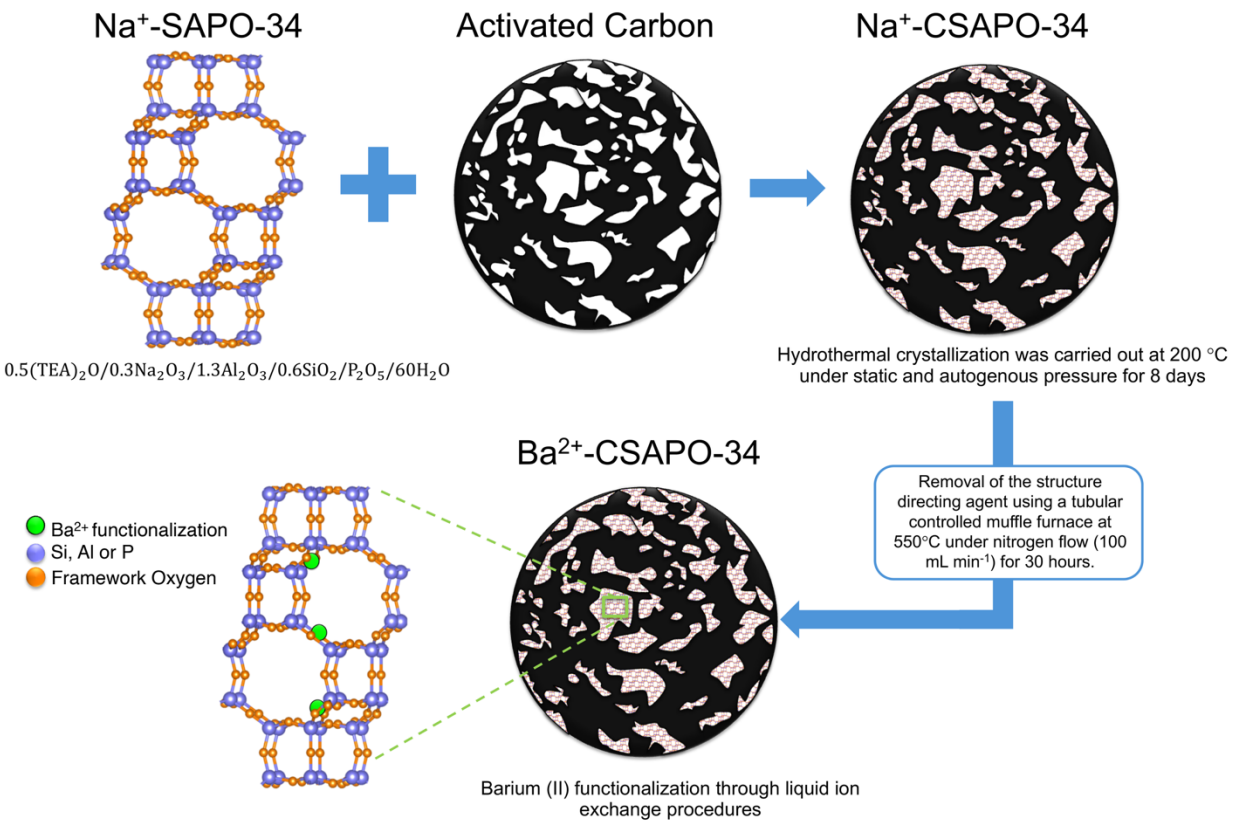

Fig. S1. Schematic summary of composite confined-space synthesis preparation.

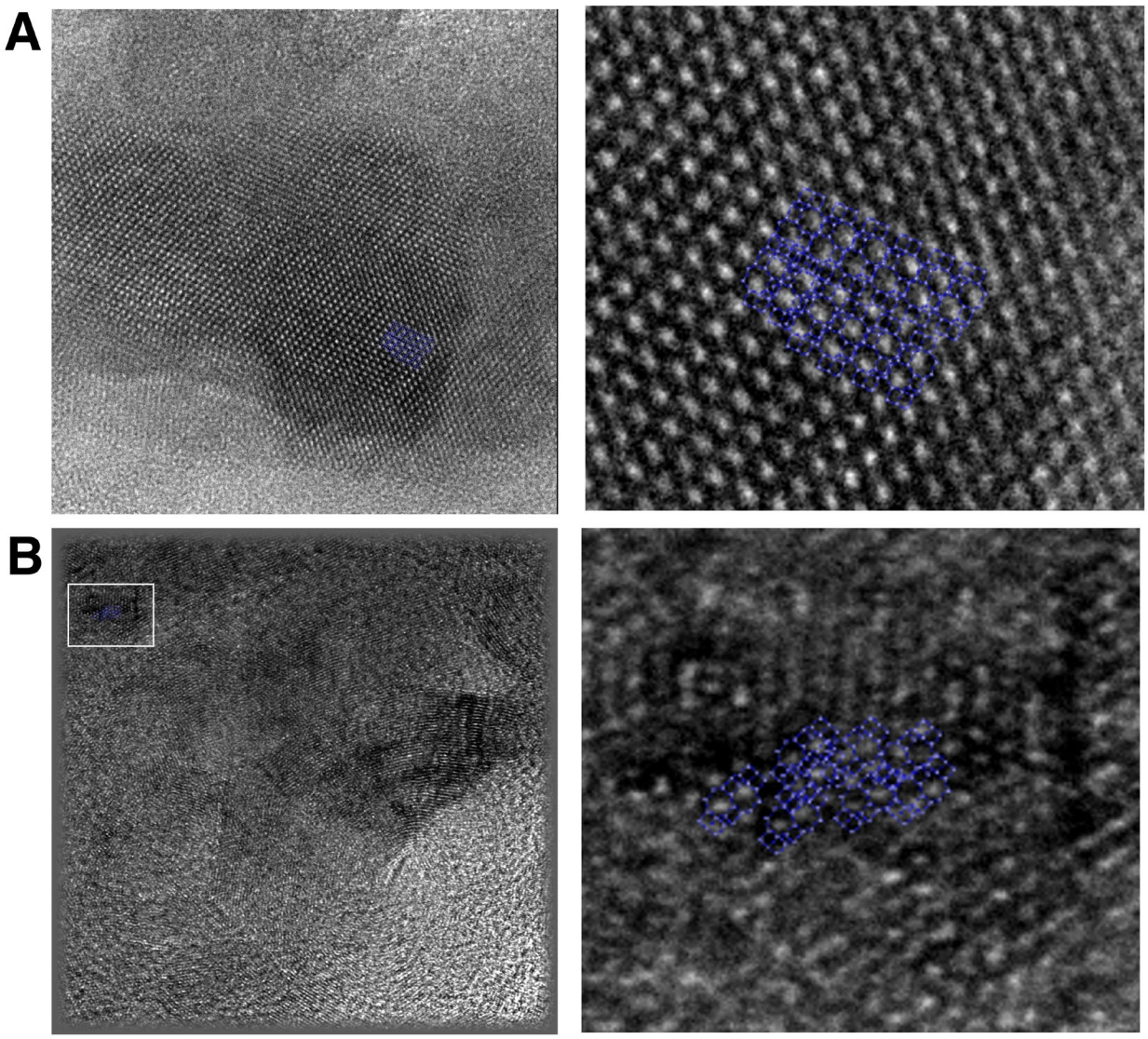

Fig. S2. TEM Imaging. (A) Ba^{2+}-SAPO-34 and (B) Ba^{2+}-CSAPO-34 TEM images (left) and magnifications with chabazite unit cell (right).

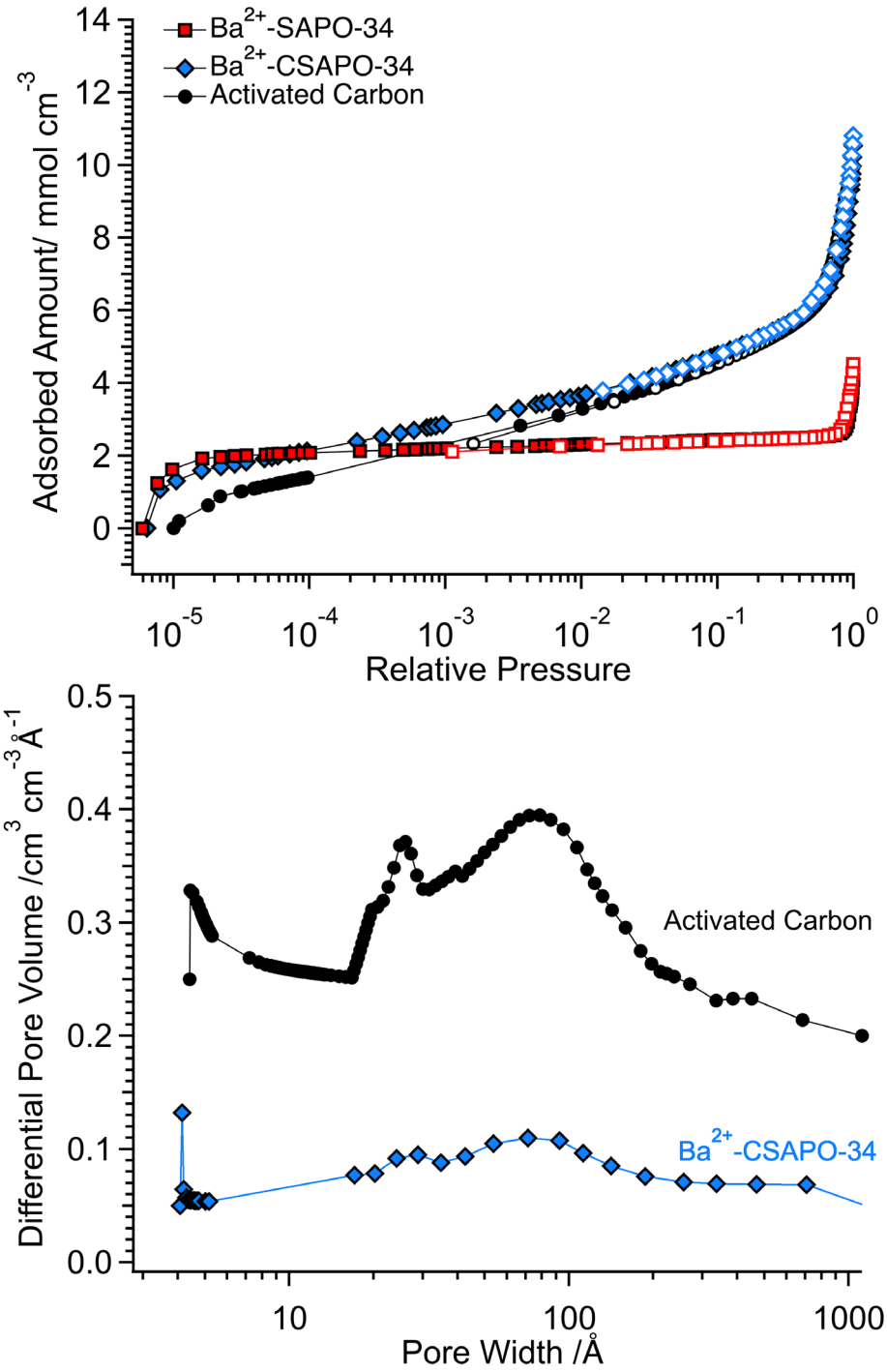

Fig. S3. Nitrogen pure component equilibrium adsorption/desorption isotherms gathered at -196 °C (77K) (*top*) and pore size distribution (PSD) profiles (*bottom*) for adsorbent materials. Corrected Horvath Kawazoe method with the Chen–Yang correction was employed to estimate PSD micropore regions, while the Barrett–Joyner–Halenda (BJH) was used to estimate meso- and macropore regions.

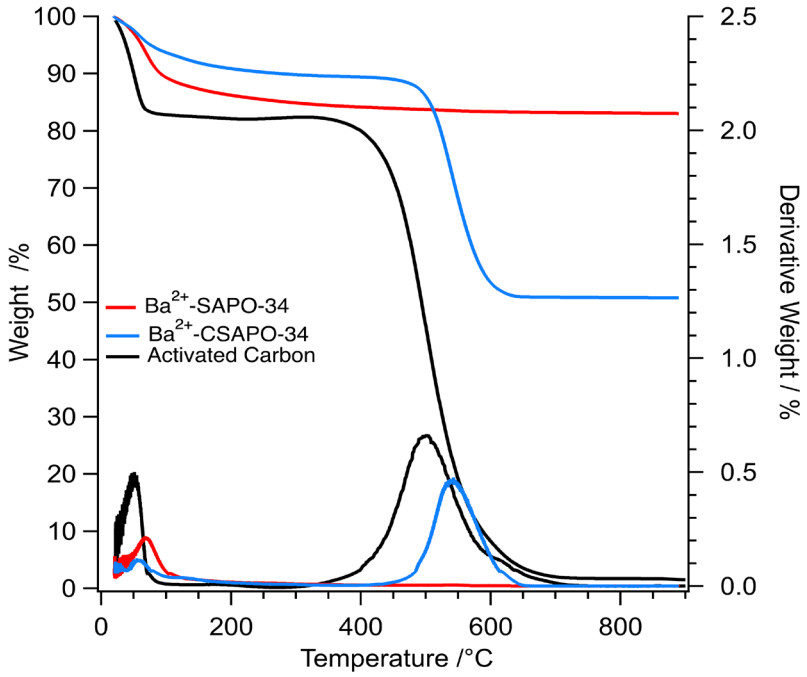

Fig. S4. Thermal gravimetric analysis and derivative weight loss profiles for detemplated and ion-exchanged materials. Data were gathered under air atmosphere using a ramp rate of 15°C/min.

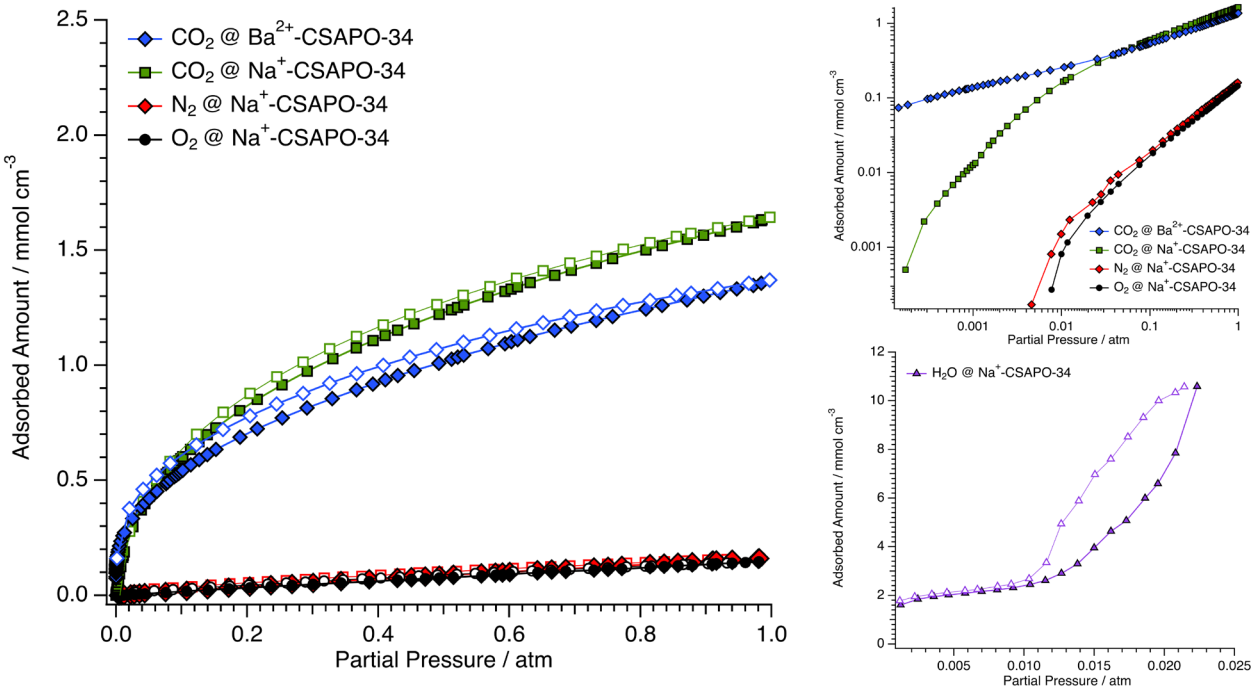

Fig. S5. CO_2, N_2, O_2, and H_2O vapor pure component equilibrium adsorption and desorption data gathered at 25 ℃ for Na^+-CSAPO-34. For reference, data also include CO_2 uptake data for Ba^{2+}-CSAPO-34. Adsorption and desorption data are depicted by closed and open markers, respectively. Loadings were normalized by volume of adsorbent instead of weight to consider differences in bulk density of each phase in the composite. Log scale plot shown in the upper-right corner.

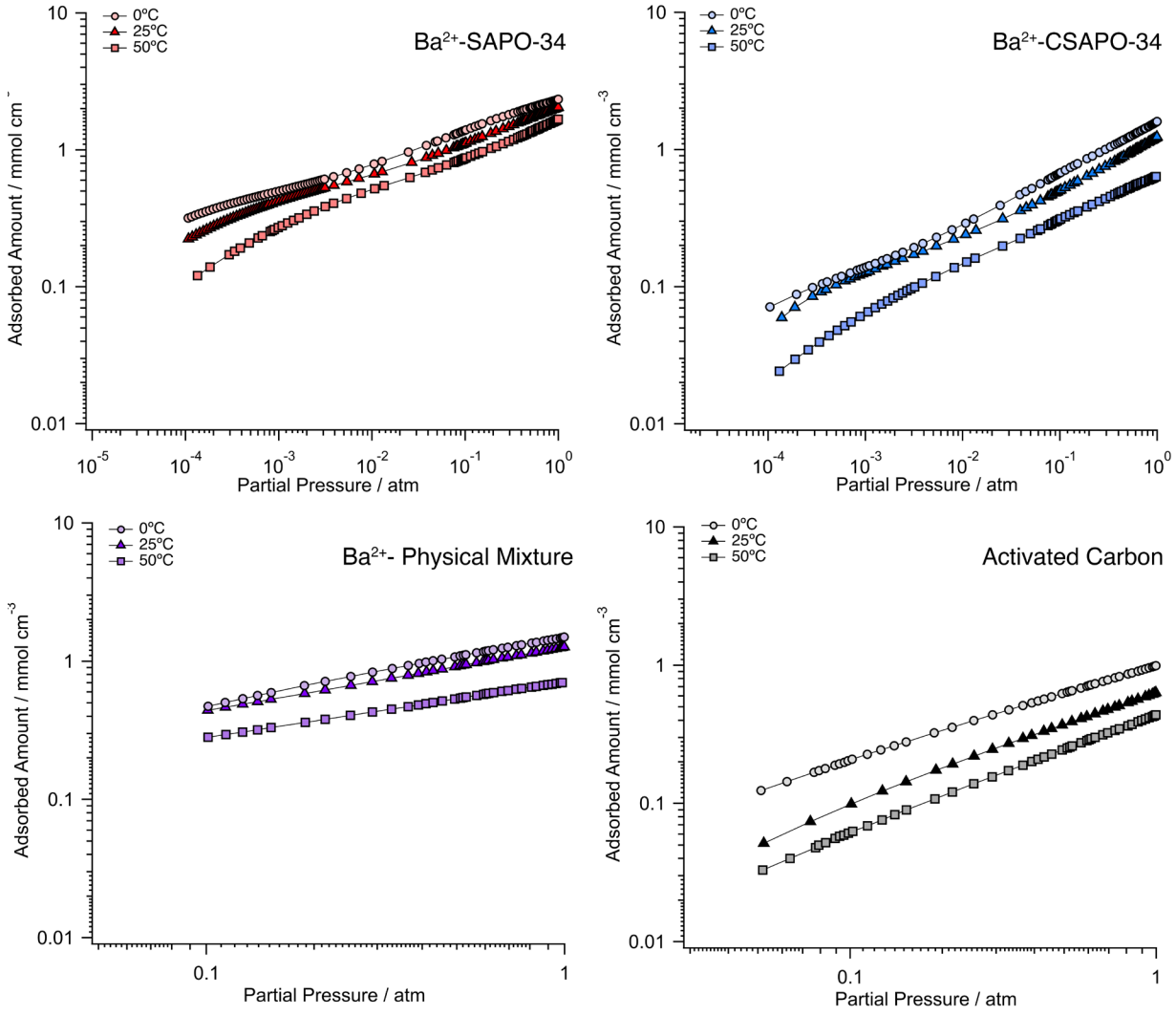

Fig. S6. CO_2 pure component equilibrium adsorption data gathered at different temperatures. All presentations are on a log scale.

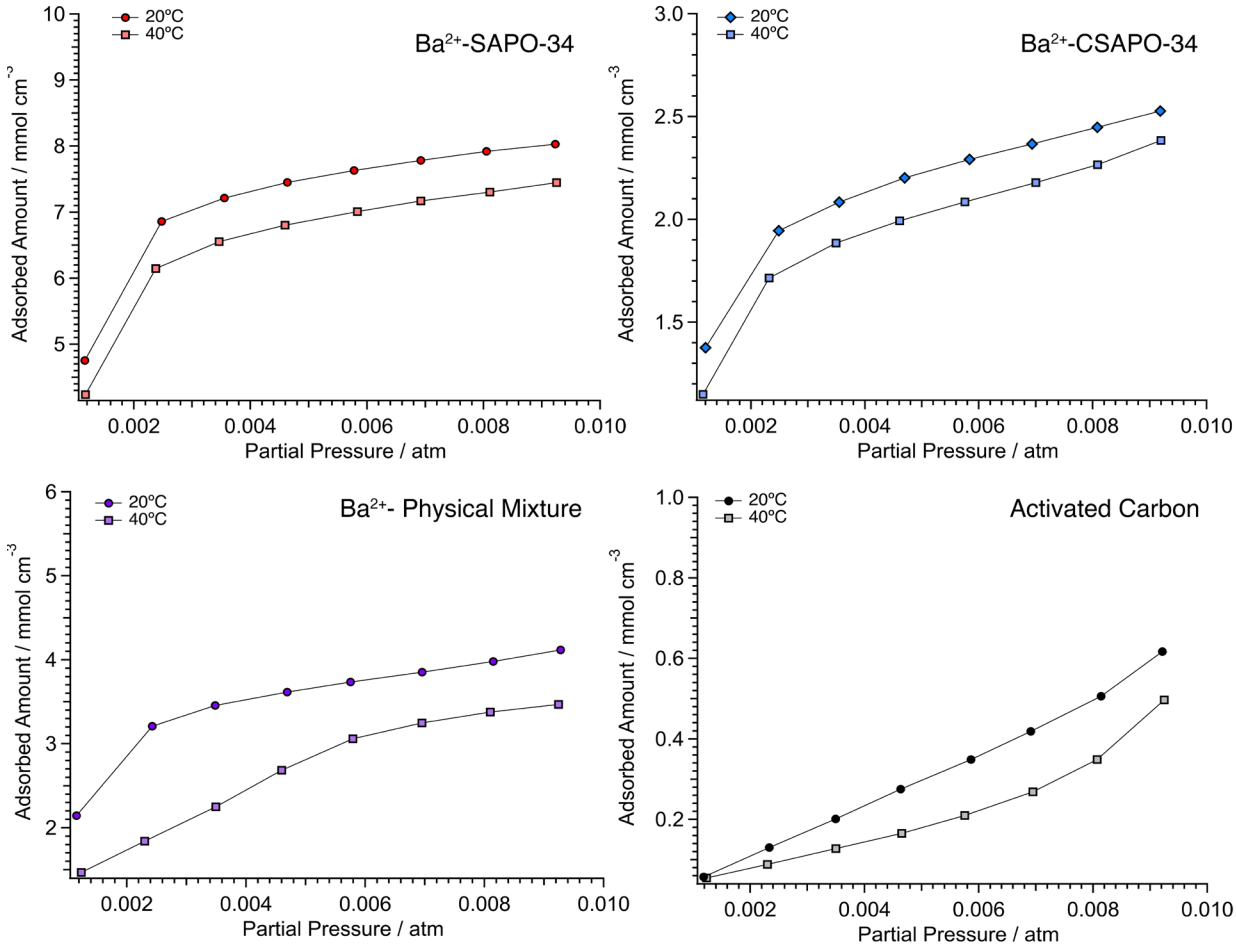

Fig. S7. H_2O vapor pure component equilibrium adsorption data gathered at different temperatures.

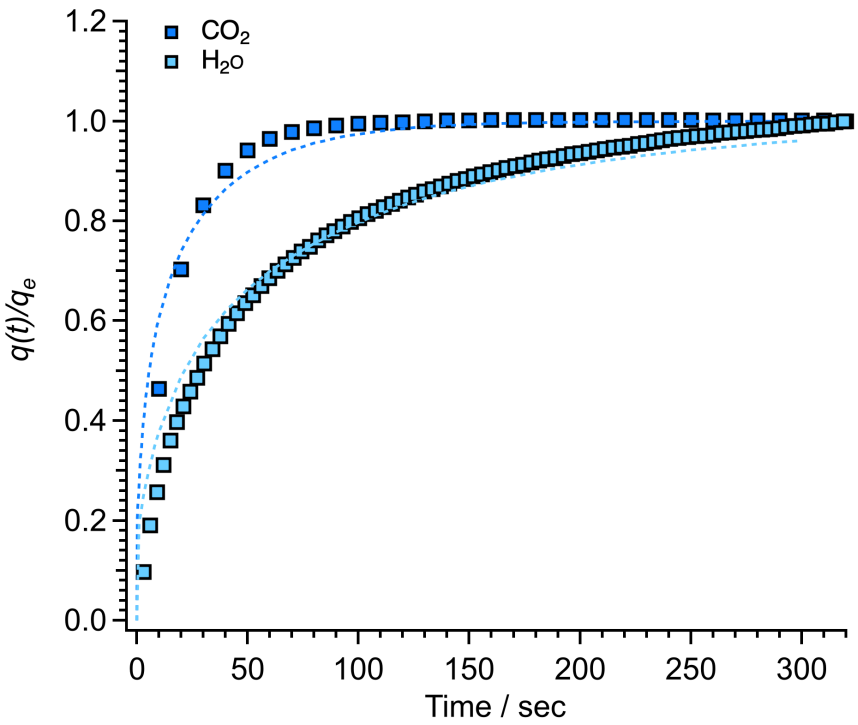

Fig. S8. Experimental and predicted CO_2 and H_2O fractional uptake for Ba^{2+}-CSAPO-34. Data were obtained at 25 °C and a CO_2 and H_2O differential pressure of approximately 0.0005 atm and 0.018 atm, respectively. The dashed lines represent a fit with the transport phenological model for spherical-shaped particles (see Eqn. S10).

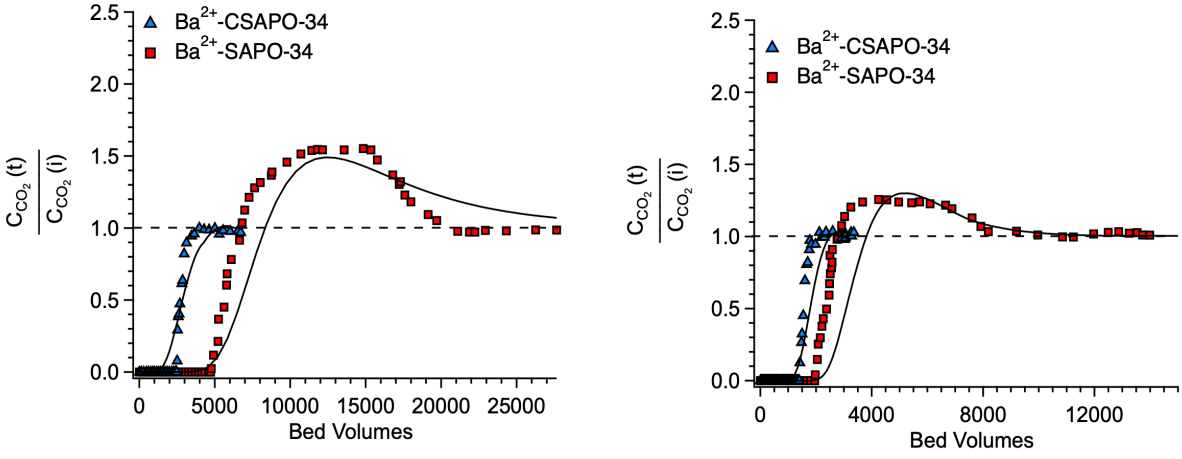

Fig. S9. Carbon dioxide breakthrough curves for humid nitrogen with an inlet concentration of 1,000 ppm (left) and 2,500 ppm (right). Continuous solid lines represent phenomenological modeling. Data were gathered using nitrogen with a relative humidity (RH) of 90%. CO_2 detection limit was 100 ppb and L = 7.62 cm.

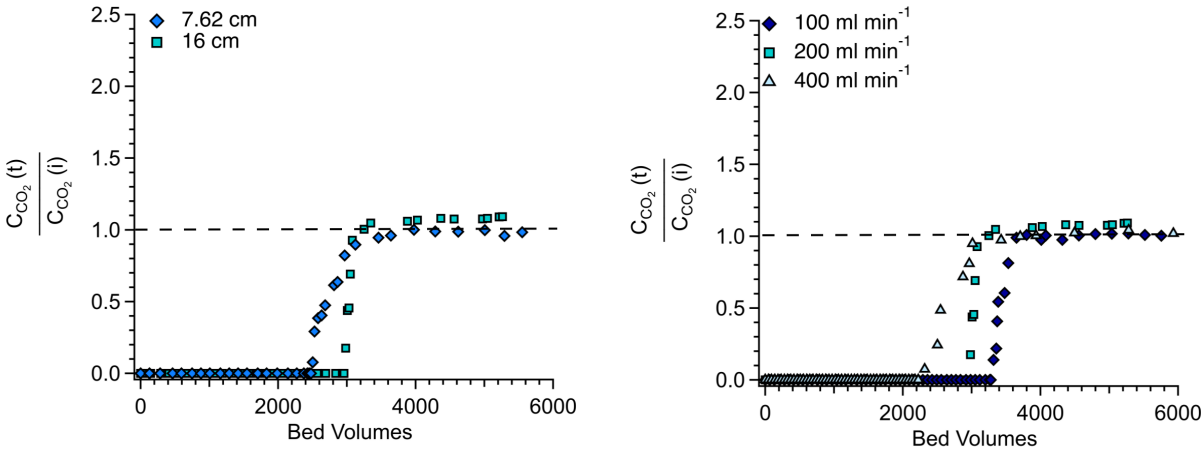

Fig. S10. Carbon dioxide breakthrough curves from humid nitrogen at two different composite bed lengths (left), and at various flow rates using a bed length of 16 cm (right). In all cases, the inlet CO_2 concentration was 1000 ppm. Data were gathered using nitrogen containing 90% relative humidity (RH). CO_2 detection limit was 100 ppb.

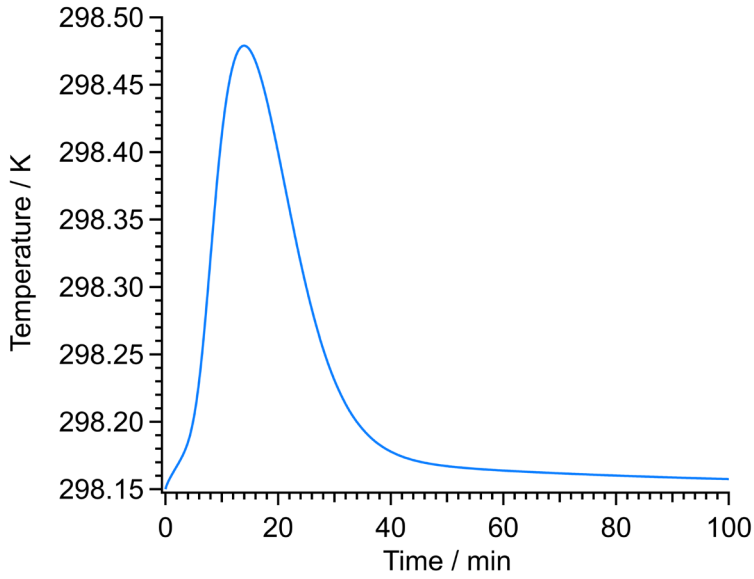

Fig. S11. Temperature profile evolution during Ba^{2+}-CSAPO-34 breakthrough curve phenomenological modeling. Data gathered for a CO_2 inlet concentration of 500 ppm at a relative humidity of 90%.

Table S1. *Unit cell composition according to energy dispersive analysis by X-ray spectroscopy (EDS) mapping and ICP-OES analysis, respectively.*

	EDS		ICP		Absolute Difference per Al
Element	**at.%**	**Ratio per Al**	**at.%**	**Ratio per Al**	
Phosphorous	14.3852	0.7922	12.7635	0.7029	0.0893
Barium	1.6284	0.0897	1.2883	0.0709	0.0187
Sodium	0.2851	0.0157	0.3603	0.0198	0.0041
Oxygen	65.5438	3.6097	67.4299	3.7135	0.1037
Aluminium	18.1575	1.0000	18.1581	1.0000	--

Table S2. Selected properties of adsorbates. [8]

Properties	**CO_2**	**H_2O**	**N_2**	**O_2**
Kinetic diameter (Å)	3.30	2.65	3.64	3.46
Quadrupole moment ($erg^{1/2}cm^{5/2}$)	-4.3×10^{-26}	~0	-1.5×10^{-26}	-0.4×10^{-26}
Polarizability ($cm^3/molec$)	2.91×10^{-24}	1.45×10^{-24}	1.76×10^{-24}	2.5×10^{-24}
Permanent Dipole (Debye)	0	1.84	0	0

Table S3. Diffusion time constants for different adsorbent materials. Data were obtained at 25 °C and a CO_2 and H_2O differential pressure of approximately 0.0005 atm and 0.018 atm, respectively.

Ads. Material	D_{s,CO_2}(1/s)	D_{s,H_2O} (1/s)
Ba^{2+}-SAPO-34	0.0019	0.00031
Activated Carbon	--*	0.0006
Ba^{2+}-CSAPO-34	0.002	0.00059

*CO_2 adsorption is negligible at the evaluated partial pressure.

Table S4. Dynamic CO_2 adsorption saturation loadings at different conditions for a bed length of 7.62 cm.

Ads. Material	**CO_2 conc. (ppm)**	**RH (%)**	**q_e± (mmol/cm³)**	**q_s± (mmol/cm³)**	**Decrease Dry to Humid (%)**
Ba^{2+}-SAPO-34	500	0	0.353	0.206	96.5
		90		0.0072	
	1000	0	0.421	0.283	90.8
		90		0.0260	
	2500	0	0.505	0.440	73.6
		90		0.116	
Ba^{2+}-CSAPO-34	500	0	0.118	0.106	8.62
		90		0.094	
	1000	0	0.143	0.138	16.6
		90		0.115	
	2500	0	0.175	0.168	8.92
		90		0.153	

±q_e and q_s are the CO_2 uptake amounts at equilibrium obtained from the isotherm data and bed saturation, respectively.

Table S5. Estimated bed capacities during dynamic adsorption at different conditions.

Flow rate (ml min^{-1})	Bed Length (cm)	CO_2 conc. (ppm)	$q_e^{\pm}$ (mmol/ cm^3)	$q_s^{\pm}$ (mmol /cm^3)	Bed Volumes
200	7.62	1000	0.143	0.115	2,503
	16			0.118	2,983
100				0.138	3,318
400				0.108	2,317

$^{\pm}$ q_e and q_s are the CO_2 uptake amounts obtained from the equilibrium isotherm data and bed saturation, respectively.

Table S6. Fixed bed saturation CO_2 adsorption capacities for treatment under dry and humid conditions and ambient temperature for various adsorbent materials.

Ads. Material	CO_2 (ppm)	Treatment Conditions	q_s (mmol/cm^3) (x 10^2)	Comments	Refs
Zeolite 13X	395	dry	49.0	Exhibits roll-up; ρ_F = 1.47 g/cm^3 ρ_B = 0.65 g/cm^3	[9-12]
		49% RH	0.0		
	400	dry	16.9		
		5% RH	1.0		
Li-LSX	400	dry	53.3	Exhibits roll-up; ρ_F = 1.47 g/cm^3 ρ_B = 0.65 g/cm^3	[9-11]
		49% RH	1.0		
K-LSX	400	dry	16.0		
		49% RH	2.0		
K-Merlinoite	400	dry	14.0	Exhibits roll-up; ρ_F = 2.18 g/cm^3 ρ_B ~ 1.00 g/cm^3 (approx.)	[12, 13]
		5% RH	0.1		
SBA-IMP(A)-30	400	dry	44.2	Average CO_2 adsorption decrease under humid conditions and after multiple cycles; ρ_F = 2.08 g/cm^3 ρ_B = 0.79 g/cm^3	[14, 15]
		60% RH	26.1		
SBA-SF-30	400	dry	47.4		
		60% RH	30.0		
SIFSIX-18-Ni-B	1000	dry	21.7	A polymorph phase results upon exposure to moisture; ρ_F = 1.32 g/cm^3 $\rho_B^{\dagger}$ = 0.31 g/cm^3	[16, 17]
		74% RH	9.3		
NbOFFIVE-1-Ni	1000	dry	65.0	Exhibits roll-up; ρ_F = 1.96 g/cm^3 $\rho_B^{\dagger}$ = 0.31 g/cm^3	[16-18]
		74% RH	2.4		
Sr^{2+}-CSAPO-34	500	dry	8.3	Withstands humidity, no roll-up, stable phases; $\rho_F^{\star}$ = 1.93 g/cm^3 ρ_B = 0.82 g/cm^3	[19]
		90% RH	2.4		
	1000	dry	10.9		
		90% RH	11.0		

Ads. Material	CO_2 (ppm)	Treatment Conditions	q_s (mmol/cm^3) (x 10^2)	Comments	Refs
Ba^{2+}-CSAPO-34	500	dry	10.6	Withstands humidity, no roll-up, stable phases; ρ_F* = 1.93 g/cm^3 ρ_B = 0.82 g/cm^3	This work
		90% RH	9.4		
	1000	dry	13.8		
		90% RH	11.5		
Ba^{2+}-SAPO-34	500	dry	20.6	Exhibits roll-up; ρ_F* =1.93 g/cm^3 ρ_B = 0.81 g/cm^3	
		90% RH	0.7		
	1000	dry	28.3		
		90% RH	2.6		

† Average bulk density estimated from data for several MOFs reported by Decker and Bloch.
‡ ρ_F and ρ_B are the adsorbent material framework and pellet bulk densities, respectively.
* SAPO phase framework density

Table S7. Comparison of experimental and phenomenological modeling data.

Ads. Material	CO_2 conc. (ppm)	Data	Adsorbate	Bed Volumes*	q_b (mmol/cm^3)*
Ba^{2+}-CSAPO-34	500	Experimental	CO_2	2,221	0.0449
			H_2O	250	0.274
		Model	CO_2	2,126	0.0427
			H_2O	229	0.251

*Estimated at breakthrough point, $\frac{C_t}{C_i} > 0$

Table S8. Summary parameters used for dynamic simulations.

Parameter	Value
DAC Simulation	
CO_2 inlet concentration (ppm)	500
Bed length (m)	0.05
Bed diameter (m)	0.01
Volumetric flowrate (L/min)	0.132
Air velocity through adsorbent layer (m/s)	0.028
Closed-Loop Simulation	
CO_2 inlet concentration (ppm)	1000 or 2500
Bed length (m)	0.254
Bed diameter (m)	0.0476
Volumetric flowrate (L/min)	30
ε	0.35
τ	3.00
D_{s,CO_2}(m^2/s)	2.28510^{-10}
D_{s,H_2O}(m^2/s)	$6.740x10^{-11}$
D_{s,N_2}(m^2/s)	$1.023x10^{-8}$
D_{m,CO_2}(m^2/s)	$1.547x10^{-5}$
D_{m,H_2O}(m^2/s)	$2.137x10^{-5}$
D_{m,N_2}(m^2/s)	$2.035x10^{-5}$

Parameter	Value
$\Delta H_{ads,avg,CO_2}$ (kJ/mol)	31.50
$\Delta H_{ads,avg,H_2O}$ (kJ/mol)	17.04
$\Delta H_{ads,avg,N_2}$(kJ/mol)	22.03
Langmuir Parameter fitting for Ba^{2+}-CSAPO-34	
H_2O Partial Pressure (atm) q_s (mmol/g) Langmuir Parameter, K_L (1/atm) RMSE*	0.016 5.3 335.9623 0.344
H_2O Partial Pressure (atm) q_s (mmol/g) Langmuir Parameter, K_L (1/atm) RMSE*	0.018 11.35 68.81 0.679
H_2O Partial Pressure (atm) q_s (mmol/g) Langmuir Parameter, K_L (1/atm) RMSE*	0.022 11.35 196.78 1.21
CO_2 Partial Pressure (atm) q_s (mmol/g) Langmuir Parameter, K_L (1/atm) RMSE*	0.001 0.3 2347.16 0.015
N_2 Partial Pressure (atm) q_s (mmol/g) Langmuir Parameter, K_L (1/atm) RMSE*	0.98 0.9 0.2529 0.0007

* Residual Root Mean Square Error

References

[1] N. Wakao, T. Funazkri, Effect of fluid dispersion coefficients on particle-to-fluid mass transfer coefficients in packed beds: Correlation of sherwood numbers, Chem. Eng. Sci. 33(10) (1978) 1375–1384. https://doi.org/10.1016/0009-2509(78)85120-3

[2] R.T. Yang, Gas separation by adsorption processes, World Scientific 1997

[3] E.L. Cussler, Diffusion: Mass Transfer in Fluid Systems, 2nd ed., Cambridge University Press, New York, 1997

[4] J. Crank, The Mathematics of Diffusion, Oxford University Press 1980

[5] C.-H. Li, B.A. Finlayson, Heat transfer in packed beds—a reevaluation, Chem. Eng. Sci. 32(9) (1977) 1055–1066. https://doi.org/10.1016/0009-2509(77)80143-7

[6] N. Wakao, S. Kaguei, T. Funazkri, Effect of fluid dispersion coefficients on particle-to-fluid heat transfer coefficients in packed beds: Correlation of nusselt numbers, Chem. Eng. Sci. 34(3) (1979) 325–336. https://doi.org/10.1016/0009-2509(79)85064-2

[7] R. Krupiczka, Analysis of thermal conductivity in granular materials, Int. Chem. Eng. 7(1) (1967) 122

[8] R.T. Yang, Adsorbents: Fundamentals and applications 2003. https://doi.org/10.1002/047144409X

[9] A.N. Stuckert, R.T. Yang, CO_2 capture from the atmosphere and simultaneous concentration using zeolites and amine-grafted SBA-15, Environ. Sci. Technol. 45(23) (2011) 10257–10264. https://doi.org/10.1021/es202647a

[10] J.M. Kolle, M. Fayaz, A. Sayari, Understanding the effect of water on CO_2 adsorption, Chem. Rev. 121(13) (2021) 7280–7345. https://doi.org/10.1021/acs.chemrev.0c00762

[11] S. Sircar, A.L. Myers, Gas separation by zeolites., in: S.M. Auerbach, K.A. Carrado, P.K. Dutta (Eds.), Handbook of Zeolites Science and Technology, CRC Press2003, pp. 1063–1105. https://doi.org/10.1201/9780203911167

[12] I. Lyadov, M. Lusardi, Characterization of K-MER and 13X zeolites for humid direct air capture of CO_2 under equilibrium and cycling conditions, Chem. Eng. J. 524 (2025). https://doi.org/10.1016/j.cej.2025.168648

[13] G. Gatta, N. Rotiroti, D. Bersani, F. Bellatreccia, G. Della Ventura, S. Rizzato, A multi-methodological study of the (K,Ca)-variety of the zeolite merlinoite, Mineral. Mag. 79(7) (2015) 1755–1767. https://doi.org/10.1180/minmag.2015.079.7.03

[14] J. Li, N. Tsunoji, M. Sadakane, Solvent-free synthesis of amine-grafted adsorbent for direct air capture, RSC Adv. 15(47) (2025) 39672–39676. https://doi.org/10.1039/d5ra03355a

[15] Y. Liu, Z. Li, X. Yang, Y. Xing, C. Tsai, Q. Yang, Z. Wang, R. Yang, Performance of mesoporous silicas (MCM-41 and SBA-15) and carbon (CMK-3) in the removal of gas-phase naphthalene: adsorption capacity, rate and regenerability, RSC Adv. 6(25) (2016) 21193–21203. https://doi.org/10.1039/c5ra27289k

[16] S. Mukherjee, N. Sikdar, D. O'Nolan, D.M. Franz, V. Gascón, A. Kumar, N. Kumar, H.S. Scott, D.G. Madden, P.E. Kruger, B. Space, M.J. Zaworotko, Trace CO_2 capture by an ultramicroporous physisorbent with low water affinity, Science Advances 5(11) (2019) eaax9171. https://doi.org/10.1126/sciadv.aax9171

[17] G.E. Decker, E.D. Bloch, Using helium pycnometry to study the apparent densities of metal–organic frameworks, ACS Appl. Mater. Interfaces 13(44) (2021) 51925–51932. https://doi.org/10.1021/acsami.1c07304
[18] P.M. Bhatt, Y. Belmabkhout, A. Cadiau, K. Adil, O. Shekhah, A. Shkurenko, L.J. Barbour, M. Eddaoudi, A fine-tuned fluorinated MOF addresses the needs for trace CO_2 removal and air capture using physisorption, Journal of the American Chemical Society 138(29) (2016) 9301–9307. https://doi.org/10.1021/jacs.6b05345
[19] G.C. del Valle-Pérez, J.C. Muñoz-Senmache, P.E. Cruz-Tato, E. Nicolau, A.J. Hernández-Maldonado, Carbon Dioxide Removal from Humid Atmosphere by a Porous Hierarchical Silicoaluminophosphate/Carbon Composite Adsorbent, ACS Appl. Eng. Mater. 1(2) (2023) 790–801. https://doi.org/10.1021/acsaenm.2c00208